Applications of Optical Fiber Sensors with Thick Metal Coatings

by

Stephen H. Poland

Thesis submitted to the Faculty of the Virginia Polytechnic Institute and State University in partial fulfillment of the requirements for the degree of

MASTER OF SCIENCE

in

Electrical Engineering

APPROVED:

Kent A. Murphy, Chairman

Richard O. Claus

Kenneth Shaw

May, 1994

Blacksburg, Virginia

Applications of Optical Fiber Sensors with Thick Metal Coatings

by

Stephen H. Poland

Kent A. Murphy, Chairman

Electrical Engineering

Over the past decade, fiber optic strain sensors have begun to transition from use in laboratory research to commercial sector applications. This transition is somewhat hindered due to the high cost associated with many optical components required for fiber optic-based sensing systems. Multiplexing systems for fiber optic sensors are one approach to reducing the per-channel cost of fiber optic sensor implementation, however, in many applications, on-line monitoring of sensor elements is not required and the periodical addressing of sensor elements is acceptable. Commercially available fiber optic strain sensor systems are now available which support periodical sensor addressing by providing absolute information about the strain state of the sensor.

A post-damage inspection fiber optic sensor design which employs a thick metal coating to retain information regarding the strain history of a sensor is demonstrated. Additionally demonstrated is a corrosion sensing technique which exploits the residual strain retention of the post-damage inspection sensor. Finally, the temperature sensing properties of the metal-coated sensor is investigated.

Acknowledgments

I would like to thank Dr. Kent Murphy, Dr. Richard Claus and Dr. Kenneth Shaw for supervising this work. I would also like to thank David Sherrer and Jason Zeakes for their important contributions to this research via their thorough knowledge of optical fiber coating technologies. I would especially like to thank Mark Alcock for supporting this research through his expertise in optical fiber sensor fabrication and his friendship. My heartfelt appreciation goes to Russ May, who is both my mentor and friend, and the primary contributor to my academic, professional, and personal growth during the last few years.

I would also like to thank my parents, Jim and Carole Poland, whose moral (and financial) support have made this possible. I am also forever in debt to my grandmother, Bernice Anthony, who always knew I had it in me. I would finally like to thank my wife, Sally, who has endured with me the long hours and non-existent weekends over the past year, and will be happy that I no longer can make any excuses about not doing my laundry.

Table of Contents

List of Illustrations

List of Tables

Chapter 1 - Introduction

Optical fiber sensors capable of measuring strain, temperature, displacement, pressure, corrosion and electric current have many advantages over their electronic counterparts [1]. The inherent immunity to electromagnetic interference afforded by optical fiber sensors permits their use in applications unavailable to electrical sensors. Additionally, high bandwidth, small size, high resolution and light weight make them ideal for the unobtrusive measurement of material and environmental physical parameters.

The purpose of the work presented in thesis is to provide the preliminary experimental characterization of a fiber optic post-damage inspection sensor, fiber optic corrosion sensor, and fiber optic temperature sensor which all utilize a thick metal coating on the sensor element as an operational basis. The goal of the post-damage inspection sensor design is to create a strain sensing element which, due to the physical characteristics of the thick metal coating, will retain information regarding large strain excursions the sensor experiences after the large strain event has occurred. It will be shown that, for a given coating thickness, the residual strain retained by the metal coated post-damage inspection sensor is a function of the peak strain experienced by the sensor. Using these results, a fiber optic corrosion sensing technique will be presented which again relies on the retention of residual strains by the thick metal coating surrounding the sensor. It will be shown that if the metal sensor coating is plastically deformed and subsequently introduced to a corrosive environment, as the coating material corrodes and its effective thickness decreases, a detectable relaxation in the residual strains experienced by the sensor will result and a corrosion sensor can be fabricated. Finally, the ability of the thick metal-coated sensor to function as a temperature sensing element will be explored.

Section 1.1 provides a brief overview of the different classes of optical fiber sensors. Section 1.2 discusses an interferometric-based fiber optic sensor, the extrinsic Fabry-Perot interferometric (EFPI) fiber optic sensor, which was used in this research. Section 1.3 overviews the approach taken to construct fiber optic post-damage inspection, corrosion, and temperature sensors based on the EFPI.

1.1 Optical Fiber Sensors

Over the past decade, fiber optic sensors have begun to transition from use in laboratory research to commercial sector applications. Optical fiber sensors are devices for measuring strain, temperature, displacement, pressure, electric currents, magnetic fields and various other material and environmental properties [1]. The general principle behind fiber optic sensing is quite simple. In communications applications, it is undesirable for the lightwaves being sent through an optical fiber to be affected by the environment, or the message being sent may be corrupted. A fiber optic sensor monitors the effect(s) that a selected environmental property has on light being sent through an optical fiber. Therefore, by measuring changes in the light exiting the optical fiber "sensor," the property of the environment that caused the change can also be measured.

There are many different classes of optical fiber sensors, with each class exploiting the way, or ways, in which the environment affects the light propagating sensor element. Perhaps the most simple of these fiber optic sensing techniques is the extrinsic air-gap intensity-based sensor in which only the attenuation of the light passing through the sensor is monitored [2]. Intensity-based sensors afford extremely simple signal processing requirements and are highly economical, but are primarily useful in two-state detection schemes or position sensing applications where very low resolution is required [2].

An intensity-based sensor which offers an improvement in resolution over the extrinsic air-gap intensity-based sensor is the microbend sensor. Although a relatively low-cost sensing approach [2], the microbend sensor is inherently lead sensitive due to the use of multimode optical fiber and they require critical alignment of the deformer mechanisms which induce the optical signal attenuation [3]. Optical time-domain reflectometry (OTDR) techniques are attractive for many fiber optic sensing applications in which a distributed sensor type is desired. OTDR sensing is undesirable for the applications discussed here due to the high-expense associated with high-resolution OTDR systems necessary for point sensing applications. In addition to the sensor types thus far discussed, there are a variety of sensing techniques reliant on polarization modulation or modal domain modulation, but these techniques typically require expensive "specialty" optical fibers, offer a high degree of lead sensitivity, or are not well suited for performing high-resolution strain measurements [2].

A particularly attractive class of sensors for a variety of applications requiring high-resolution and lead-insensitive measurements is that of the phase modulated, or interferometric-based, optical fiber sensors. Interferometric-based sensing techniques rely on the phase modulation of light propagating through an optical fiber. The induced phase modulation is measured by splitting the light propagating through the optical fiber into two (or more) beams, modulating the optical path length along one (or both) of the beams, and then recombining the beams and allowing them to interfere. The result is a sinusoidally varying intensity variation of the recombined light signal as a function of the induced optical path length change. The geometries of interferometric sensors are generally separated into Mach-Zehnder, Michelson, and Fabry-Perot topologies. The Mach-Zehnder interferometer is likely the most widely researched fiber interferometer class due to its easy construction [4]. However, the Mach-Zehnder and Michelson techniques do not offer the geometrical implementation flexibility of the Fabry-Perot techniques since both the Mach-Zehnder and Michelson fiber interferometers both require both a sensing and reference fiber in their construction. This lack of implementation flexibility is primarily because optimal operation of the Mach-Zehnder and Michelson interferometers requires environmental isolation of the fiber reference leg of the sensor. Additional benefits of Fabry-Perot fiber interferometers over the Mach-Zehnder and Michelson fiber interferometers is the reduced requirements on source coherence length dictated by the Fabry-Perot, and, due to the physical construction of the Fabry-Perot, the ability of the Fabry-Perot to more closely resemble a point sensor.

1.2 Extrinsic Fabry-Perot Interferometric Optical Fiber Sensors

Two classes of fiber Fabry-Perot interferometers exist, these being the intrinsic and extrinsic varieties. In the intrinsic case, reflector sites are introduced in the optical fiber and phase modulation of the light signal occurs between two reflector sites. The weakness of the intrinsic design is that the phase of the light propagating between the reflector sites is not only affected by the path length of the light, but transverse strains introduced to the optical fiber between reflector sites. In contrast, the extrinsic design insures only displacements in the axial direction of the sensor will affect the sensor output. The transverse strain dependence in the intrinsic design occurs due to the functional dependence between the index of refraction of the optical fiber and the strain state of the fiber; hence, as the length of optical fiber between the reflector sites is mechanically or thermally strained, a change in the speed of the light propagating through fiber results and phase modulation of the light signal occurs. This problem is avoided in the extrinsic sensor design because there is only air between the reflector sites, and transverse strains will have no affect on the propagation of the light through the sensor element. The intrinsic Fabry-Perot interferometer is inherently susceptible to measurement cross-sensitivity because the response of the sensor is affected by sensor straining in all directions which is undesirable since the manifestation of these different strain vectors in the sensor output cannot be separated without the use of expensive "specialty" optical fibers [5].

The extrinsic Fabry-Perot interferometric (EFPI) fiber optic sensor, developed and patented by the Fiber & Electro-Optics Research Center (FEORC) at Virginia Tech has been used for the quantitative analysis of materials and structures [6-8]. Using the basic EFPI sensor geometry, short gage length displacement and strain sensors have been implemented [9]. Sections 1.2.1 and 1.2.2 discuss differential and absolute operation of EFPI sensor elements. Section 1.2.3 discusses how the EFPI sensor data is interpreted to acquire quantitative strain measurements.

1.2.1 Differential Measurement Technique Using EFPI Sensors

For relative, or differential operation of the EFPI, a singlemode optical fiber with a cutoff wavelength of 1270 nanometers transmits light from a laser diode to the sensor element. At the opposite end of the input fiber, the laser light signal is partially reflected and partially transmitted across the gap separating the ends of the input fiber and the reflector fiber. The signal reflected from the reflecting fiber and the signal reflected from the facing fiber endface interfere and propagate back through the input fiber to a photodiode detector.

The detected photodiode signal current is proportional to the phase difference between the two reflected optical fields [7]. Assume a coherent, approximately plane wave detected at the output of the sensor. This wave can be represented by [7]

$$_{i}(x,z,t) = A_i \exp(j\phi_i), \qquad \text{i=1,2,} \tag{1.1}$$

where the variable A_i is a function o the transverse coordinate and the distance traveled, z, and the subscripts i = 1,2, stand for the reference and the sensing reflections, respectively. Assuming that the reference reflection A_1 = A, the sensing reflection A_2 can be approximated by the simplified relation [7]

$$A_2 = A\left\{\frac{\mathrm{ta}}{\mathrm{a} + 2\mathrm{s}\tan\left[\sin^{-1}(NA)\right]}\right\}, \tag{1.2}$$

where a is the fiber core radius, t is the transmission coefficient of the air-glass interface (≈0.98), s is the end separation of the two fibers, and NA is he numerical aperture of the singlemode fiber. The observed intensity at the detector is a superposition of the two amplitudes and is given by [7]

$$\mathrm{I}_{\det} = \mathrm{A}_{\det} = \left|\mathrm{U}_1 + \mathrm{U}_2\right|^2 = \mathrm{A}_1^2 + \mathrm{A}_2^2 + 2\mathrm{A}_1\mathrm{A}_2\cos(\phi_1 - \phi_2), \tag{1.3a}$$

which can be rewritten as [7]

$$I_{det} = A^2\left(1+\frac{2ta}{a+2s\tan\left[\sin^{-1}(NA)\right]}\cos\left(\frac{4\pi\cdot s}{\lambda}\right)+\left\{\frac{ta}{a+2s\tan\left[\sin^{-1}(NA)\right]}\right\}^2\right), \quad (1.3b)$$

where it is assumed that $\phi_1 = 0$ and $\phi_2 = 2s(2\pi/\lambda)$, and that λ is the source wavelength in free space. The simplified loss relation in Equation 1.3b is sufficient to understand the operation of the EFPI sensor. Changes in the gap separation distance, s, between the surfaces of the fibers aligned in the support tube produce a modulation of the output signal current. This modulation is sinusoidal, gradually decreasing in amplitude as the gap separation, s, increases. The gage length of the EFPI sensor, L_o, is defined as shown in Figure 1.1, between the two adhesive points in the hollow-core silica tube. In practice, the gage length may be set during fabrication to be several millimeters or less. The differential EFPI support system used in the research conducted for this thesis provides a theoretical measurement resolution of 0.3 nanometers.

1.2.2 Absolute Measurement Technique Using Broadband Source

In addition to differential operation of the EFPI fiber optic sensor, absolute measurement of the gap displacement, *s*, may be achieved. Absolute sensor polling allows the absolute displacement of the sensor to be determined. Absolute measurement systems which support the EFPI sensor are commercially available. In the operation of the absolute EFPI (AEFPI) systems, in place of the narrow linewidth source described in section 1.2.1, a broadband coherent source is used. At the sensor output, the intensity of multiple optical wavelengths of the broadband source are monitored by the AEFPI support system via a charge coupled device (CCD) array. Bhatia provides a thorough discussion on the theory

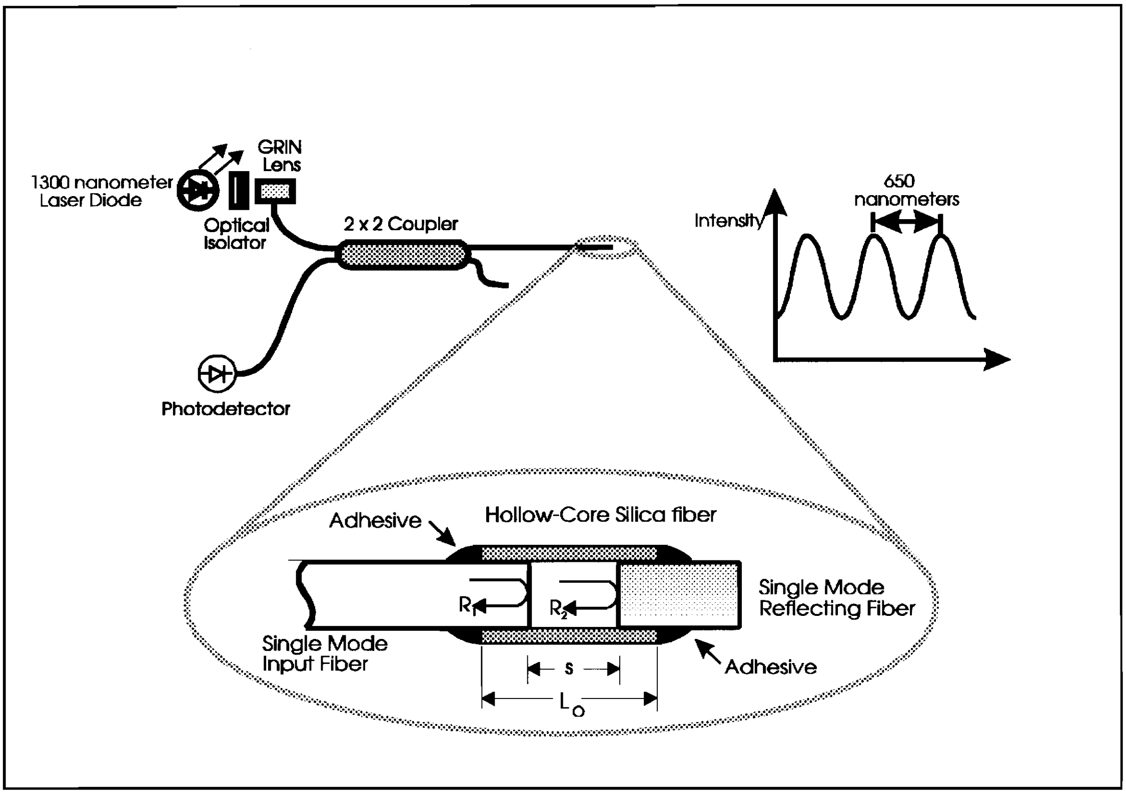

Figure 1.1. Extrinsic Fabry-Perot interferometric (EFPI) sensor system.

of operation of absolute EFPI (AEFPI) strain sensors [10]. Commercially available AEFPI systems offer a strain resolution of 40 microstrain ($\mu\varepsilon$) over a 1 centimeter gage length [11]. In the research performed for this thesis, the differential measurement technique was used to characterize the thick metal-coated EFPI sensor elements. In practice, absolute operation of the sensor elements is support the periodical addressing of the sensor elements.

1.2.3 Strain Measurement Using EFPI Sensors

As discussed in Sections 1.2.1 and 1.2.2, in both differential and absolute operation of EFPI sensors, the gap separation, s, of the sensor elements may be determined. In many applications of EFPI sensors, it is desirable to measure the strain experienced by the sensor in contrast to the gap separation. Strain describes the percentage change in the dimensions of an object. Hence, for the EFPI sensor, axial strain may be expressed as

$$\text{strain} = \varepsilon = \frac{\Delta L}{L} = \frac{\Delta s}{L_o}, \tag{1.4}$$

where Δs is the change in gap separation and L_o is the gage length of the sensor as defined in Figure 1.1. Upon fabrication of an EFPI sensor, one measures the gage length of the sensor, L_o, prior to sensor implementation. During operation of the sensor, changes in the gap separation, s, are monitored, and strain is subsequently determined using equation 1.4.

1.3 Overview

The goal of the damage sensor, corrosion sensor, and temperature sensor development was to create sensors well-suited for periodical addressing measurement applications (versus constant on-line monitoring of the sensor elements), or when it is undesirable or unnecessary to have measurement support instrumentation near the sensor during a particular event or time period of interest. The post-damage detection, corrosion, and temperature sensors are characterized via differential measurement techniques, however, in practice, absolute interrogation of the sensors would be performed.

Chapter 2 describes the plasticity and elasticity theories of metals which are exploited to create the post-damage inspection and corrosion sensors. Also provided in Chapter 2 is a discussion of candidate metal coating materials for the construction of the thick metal-coated fiber optic sensors and an overview of the application of elasticity-plasticity theory which can be used to model the sensor element when subjected to uniaxial stress/strain. The final section of Chapter 2 will provide a brief background on the corrosion of metals to establish the operational concept of the corrosion sensor. Chapter 3 discusses the coating techniques available for the fabrication of a thick metal-coated fiber optic sensor and Chapter 4 documents the fabrication process of the sensors used in this research. Chapters 5, 6 and 7 document the experimental work performed for the development of the post-damage inspection, corrosion, and temperature sensors, respectively. Finally, Chapter 8 summarizes the development of the sensors and indicates their potential uses and limitations in addition to discussing future work needed for commercial application of the thick metal coated fiber optic sensors.

Chapter 2 - Elastic-Plastic Theory and the Properties of Metals

The strength, ductility, and weldability of metals make them extremely useful in a wide range of engineering applications [11]. Of particular importance to the performed for this thesis is the ductility of metals. In essence, ductility describes the way in which a material lends itself to being permanently reshaped due to the application of stress, in other words, plastically deformed. An additional property of materials which is of interest to this research is elasticity, which describes the case in which a stress is applied to a material which causes the material to deform, but upon removal of the stress, the specimen regains the original shape. Section 2.1 of this chapter provides a fundamental theoretical perspective on elastic and plastic theory which will be a basis for development of the fiber optic-based post-damage inspection and corrosion sensors discussed in this thesis. Section 2.2 of this chapter will present basic properties of metal corrosion which are needed to evaluate the potential feasibility of the corrosion sensing technique discussed in Chapter 6.

2.1 Fundamentals of Material Deformation

Three fundamental types of material deformation are useful to describe the effects of applied mechanical stress on a material system, these are plastic, elastic and creep deformation [12]. A useful tool in the understanding of deformation theory is the use of rheological models, which mechanically describe the different classes of deformation. Figure 2.1 presents rheological models for the three deformation types [11]. It should be noted that the approximate deformation analysis that will be presented in this section will be on the macroscopic level, however, the reader should be aware that the deformation mechanics discussed in this section can be exactly characterized by examining the molecular and atomic interactions of the bulk metal material [12].

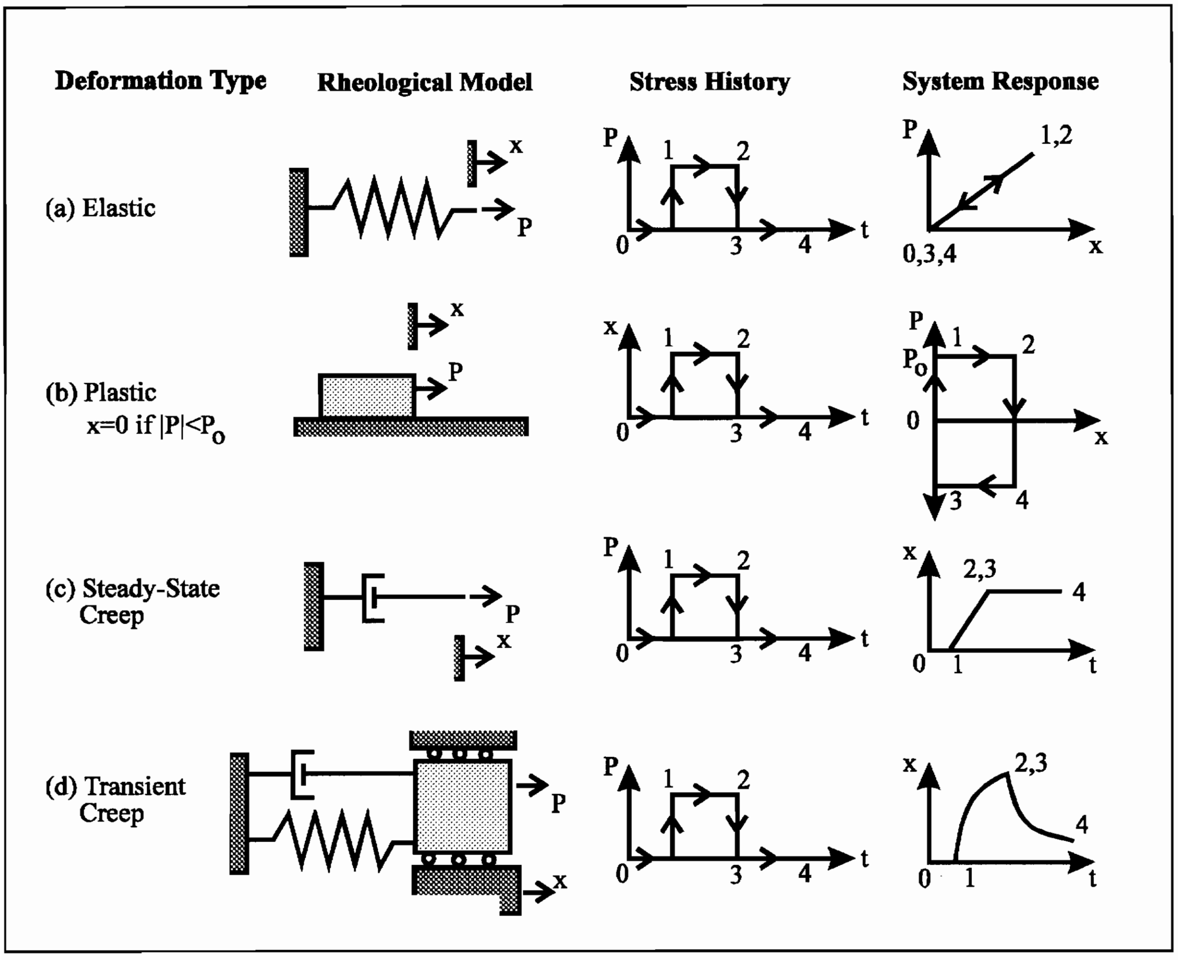

Figure 2.1 Rheological models for elastic, plastic and creep deformation. P is stress, x is the displacement of the model from the initial position or state of the model (strain), and t is time. (Adapted from Dowling [12])

As demonstrated in Figure 2.1, elastic deformation of a material is similar to stretching a spring. Once the spring is released, the original length of the spring is immediately regained. In contrast, plastic deformation can be described as the case in which a stres, is applied to a material which causes the shape of the material to permanently change. The rheological model for plasticity, shown in Figure 2.1, uses the analogy of trying to move a block on a flat surface. Due to friction between the block and the flat surface, a certain level of stress (force) is required to put the block into motion and induce a displacement. Once the stress is relaxed, the block stays where it is and does not move back to the original position the block had prior to the application of the stress.

The rheological models of elasticity and plasticity shown in Figure 2.1(a) and (b) are to be considered time independent. The time independence of the elastic and plastic deformation models can be seen in the plasticity model of Figure 2.1(b), because clearly, with no additional applied stress, the block will not move after the applied stress is removed. In the elastic case shown in Figure 2.1(a), the time indepedency is not as evident until one considers that the deformation of the material is instantaneous when stress is applied, hence, if the stress is removed, the material instantaneously returns to the original size.

Creep deformation addresses the time dependency of material deformation. Figure 2.1(c) shows the case of steady-state creep which describes the situation where a material will undergo deformation at a constant rate for a constantly applied stress; this material property is modeled by a linear dashpot. In the case of transient creep, the material deformation will not be steady due to a constant applied stress or displacement, but will slow as time passes. Additionally in the case of transient creep, once the stress is removed, the material will attempt to regain the shape that it had prior to the initial application of the stress. Clearly, the models presented in Figure 2.1 are simple tools used to describe the various deformation types, and for any given deformation event, a combination of the deformation types must be used to fully explain the event. The question therefore arises for the designer as to what degree a system must be modeled to achieve adequate insight into the system for a specific engineering application.

For the purposes of this study, it was deemed adequate to describe the mechanical performance of the thick metal-coated optical fiber sensors simply using elastic and plastic models. Therefore, the work presented here will not consider the time dependency of the sensor response to an applied stress/strain. However, the coating deformation time dependency of the post-damage inspection and corrosion sensors must be addressed prior to practical application of the sensors. Time dependency issues will be further discussed in Chapter 8. The remainder of this section will be dedicated to the development of time independent elastic-plastic material behavior which will be useful in the analysis of the post-damage inspection and corrosion sensors.

2.1.1 Elastic-Plastic Deformation

As previously mentioned, the model which will be developed to describe mechanical performance of the metal-coated sensor will contain both elastic and plastic deformation properties. To further explore this approach, Figure 2.2 shows the rheological models of four types of plastic deformation and the responses of these models to a strain event in which a material specimen was strained over a selected range, allowed to relax, and then restrained to a higher level. For the remainder of this discussion, this type of loading history will be referred to as zero-stress reloading.

Shown in Figure 2.2(a) is the rheological model for a rigid, perfectly plastic material. Rigid, perfectly plastic materials are modeled using a friction slider (in place of the block

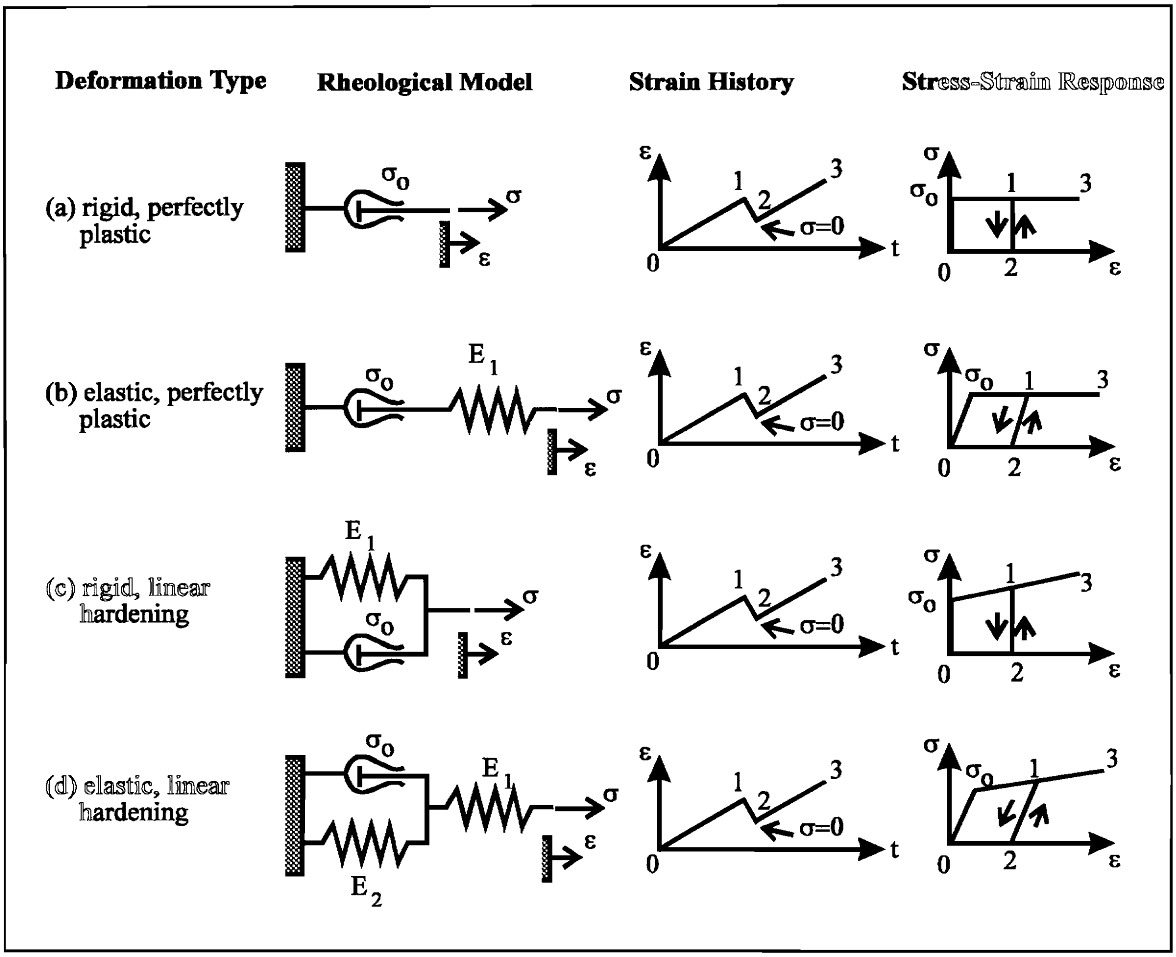

Figure 2.2. Rheological models for various types of plastic deformation. $E_{(1,2)}$ is the slope of the stress/strain relationship of the material specimen, σ_o is the yield stress of the material specimen, and σ is the applied stress. (Adapted from Dowling [12])

in Figure 2.1(b)). In the case of a rigid, plastic material, if a stress is applied, the material will resist deformation until the applied stress exceeds the yield stress, σ_o, of the material. Once σ_o has been reached, and the applied stress is released, the material will retain the deformed shape. If the stress is removed and then reapplied, the stress-strain path will be retraced vertically until the applied level of stress again exceeds the yield stress, at which point the slope of the stress/strain relationship of the material will again return to zero.

Figure 2.2(b) shows a slightly more complex modeling approach described by elastic, perfectly plastic behavior. In the rheological model for elastic, perfectly plastic behavior, a spring has been added to the rigid, perfectly plastic model, which causes the stress level to linearly increase with the applied strain, but once the yield stress level, σ_o, is reached, the system plastically deforms. Also noted in Figure 2.2(b) is that if the applied stress is released, the material will tend to regain the original shape. The rigid, linear hardening material deformation model, shown in Figure 2.2(c), is similar to the elastic, perfectly plastic deformation model, with the exception that the slope of the stress/strain relationship for the rigid, linear hardening model is non-zero after the applied stress exceeds the yield stress of the material.

The strain in the stress/strain relationship of a material may be decomposed into elastic and plastic strains, where *elastic strains are strains which are recovered by the material upon release of the applied stress*, and *plastic strains are strains which are permanent*. This decomposition of the stress-strain relationship will be used in the evaluation of the experimental results presented in Chapter 5.

The rigid, perfectly plastic, elastic, perfectly plastic, and rigid, perfectly plastic models are useful in understanding the properties of deformation mechanics, however, they fall short of adequately describing the behavior of metals which are of interest for this research. Figure 2.2(d) provides a more realistic description of the deformation properties of metals via the elastic, linear hardening model. In the case of elastic, linear hardening, the stress/strain relationship of a material is linear up to the yield stress threshold; once a level of stress is applied to the material exceeding the yield stress, σ_O, the slope of the stress/strain relationship decreases. If the applied stress is removed, an elastic strain component will be recovered as the material relaxes, but a plastic (residual) strain will remain. Furthermore, the slope of the stress-strain curve to the zero-stress level is parallel to the original loading stress/strain relationship.

A final key characteristic of the elastic, linear hardening model is observable in the stress/strain relationship when stress is repeatedly applied and removed (zero-stress reloading). The stress/strain and applied strain versus residual (plastic) strain relationships for elastic, linear hardening systems subjected to zero-stress loading events are shown in Figure 2.3(a). As shown in Figure 2.3(a), for the zero-stress reloading of elastic, linear hardening materials, the stress-strain characteristic of the material linearly increases with

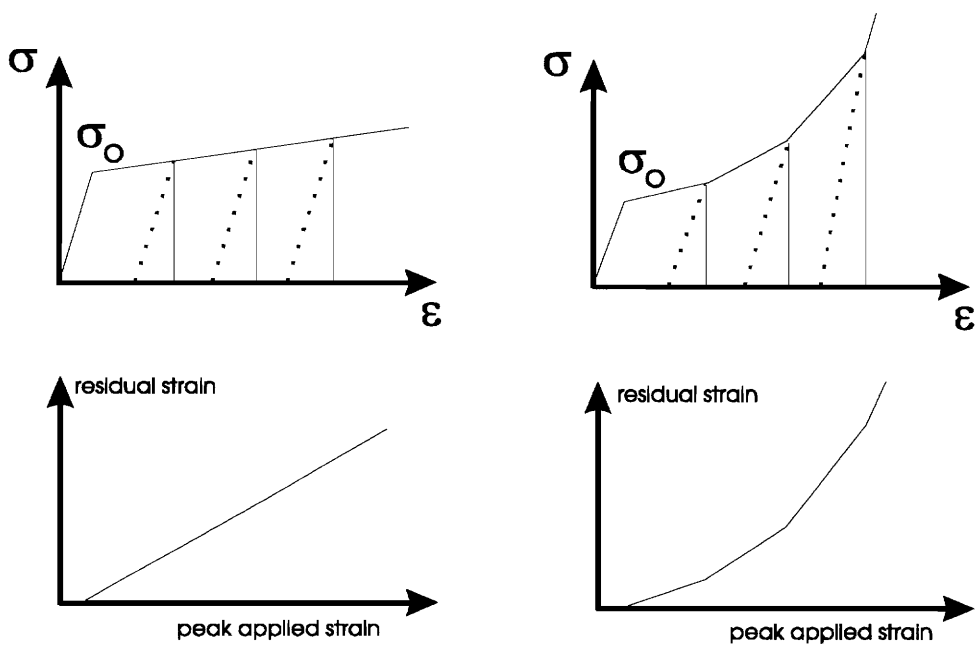

(a) elastic, linear hardening (b) elastic, non-linear hardening

Figure 2.3. Zero-stress reloading characteristics of (a) elastic, linear hardening and (b) elastic, non-linear hardening material deformation models.

the same pre-yield stress slope until the yield stress threshold is again met, at which point the stress/strain slope changes to the post-yield stress level. The lower plot in Figure 2.3(a) shows the peak applied strain versus residual strain relationship for an elastic, linear hardening material system. Figure 2.3(b) shows the stress/strain and peak applied strain versus residual strain relationships for an elastic, non-linear hardening material system in which the yield stress of the material is a function of the loading history of the material. *Note the linear peak applied strain versus residual strain relationship for elastic, linear hardening materials, but the non-linear peak applied strain versus residual strain relationship for elastic, non-linear hardening materials.* The peak applied strain versus residual strain properties of the elastic, linear and non-linear hardening deformation models for zero-stress reloading conditions is crucial to metal-coated post-damage inspection sensor development and will serve as the basis for the interpretation of the experimental work presented in Chapter 5. Section 2.1.2 discusses the physical meanings of the elastic, or Young's modulus, E, and yield stress, σ_o, discussed earlier in this section.

2.1.2 Elastic Modulus, Poisson's Ratio and the Yield Point

As shown in Figure 2.2, from an initial stress-strain state of zero, a material will exhibit a linear stress-strain relationship under the application of a stress, until the stress reaches the σ_O value. The slope of this linear stress-strain relationship is called the elastic, or Young's modulus of a material, which is typically symbolized by E. In Figure 2.2, E_1 is the elastic modulus of a material. As with E, σ_O also has a physical interpretation as the initial yield strength (yield stress threshold) of a material. Demonstrated in Figure 2.2, once the applied stress on a material exceeds the initial yield strength of the material, the slope of the stress-strain relationship is reduced.

In the plastic deformation model, the yield strength (yield stress threshold) of a material is simply stated as

$$\sigma_O = \frac{P_O}{A}, \tag{2.1}$$

where P_O is the force (see Figure 2.1) required to initiate plastic deformation in the material and A is the cross-sectional area of the specimen. A final useful material parameter which is useful in describing the performance of elastic, linear hardening plastic deformation is the Poisson's ratio of a material. Thorough development of the post-yield strength stress-strain relationship and a rigorous definition of Poisson's ratio requires a deviation from the simple uniaxial stress-strain models thus far presented. Hence, for the uniaxial modeling presented in this thesis, Poisson's ratio will simply be defined as [12]

$$\nu = -\frac{\text{transverse strain}}{\text{axial strain}}. \tag{2.2}$$

For an in-depth treatment of Poisson's ration in plasticity theory, please see Calladine [11] or Dowling [12]. Simply stated, the higher the Poisson's ratio, the more incompressible a material becomes [11]. Table 2.1 provides the Poisson's ratio, yield strength, and elastic modulii of relevant metals and silica glass.

One final note should be made in this evaluation of elastic, linear hardening materials with respect to the yield strength of a material. In reality, the yield strength of a material is a function of the loading history of the specimen. Hence, if a material specimen is loaded

Table 2.1. Relevant material parameters for selected metals and silica glass.

Material	Elastic Modulus (GPa)	Yield Strength (MPa)	Poisson's ratio
Gold	76	303	0.37
Copper	120	300	0.35
Silver	83	207	0.36
Aluminum	70	150	0.33
Silica Glass	69	-	0.19

past the initial yield strength of the specimen, and then unloaded, the stress level at which plastic deformation will again occur will be different. This deformation characteristic creates the need for the elastic, non-linear hardening model discussed in Section 2.1.1 [12]. For the purposes of the sensor development presented in this thesis, the elastic, linear hardening model will be assumed, however, prior to practical application of the post-damage inspection and corrosion sensors, an evaluation of the non-linear hardening properties of the metal-coated sensor must be performed to determine if they are significant to the operation of the individual sensor types.

The modeling approach taken by Sirkis and Dasgupta [13] to describe a metal-coated optical fiber is to describe the material system as elastic, linear hardening. For the case of the EFPI sensor, this model is not complete since the sensor is constructed from a glass capillary tube, and therefore cannot be modeled using a cylinder of silica glass, such as that used by Sirkis and Dasgupta. The complexity of thoroughly developing the stress/strain relationship of a thick metal-coated EFPI sensor is immense and beyond the scope of this thesis. However, the theoretical model of elastic/plastic-coated fiber optic sensors presented by Sirkis and Dasgupta can be used to better understand the operation the post-inspection damage sensor. Qualitatively, the theoretical work performed by Sirkis and Dasgupta state that the amount of residual strain retained by the sensor coating for a given peak strain is a function the coating material properties (Young's modulus, yield strength, and Poisson's ratio) and the coating thickness [13]. The principles of deformation which have been discussed will be used both in the design of the sensors and evaluation of the experimental work conducted with the sensor types.

2.2 Corrosion of Metals

A property which all metals have in common is the susceptibility to corrosion [14]. A large part of corrosion engineering is selecting materials for a particular environment which frustrate the corrosion process, however, eventual corrosion of the material is inevitable. Corrosion is often described by two metrics: weight change and dimensional change. The weight change associated with corrosion can be either an increase or decrease, but corrosion strictly induces a reduction in the dimensions of a material specimen [14].

Corrosion can be divided into three basic types, chemical, electrochemical, and physical, and these types are each affected by a large number of environmental factors, such as temperature, potential difference, surface condition, as well as others. Chemical corrosion is basically when a material is dissolved due to the presence of another substance. Electrochemical corrosion comes in a variety of different forms, with the commonality being the presence of an electrolytic solution, an anode (the corroding material), a cathode, and an electrical circuit [14]. Finally, physical corrosion can be described as the direct loss of mass from a material specimen via physical mechanisms excluded from the chemical and electrochemical corrosion processes.

The purpose of the research presented here is not to evaluate the performance of the proposed fiber optic corrosion sensor when faced with different corrosion types, but to establish the feasibility of the sensor design. Accordingly, rigorous treatment of corrosion is beyond the scope of this thesis. As previously stated, the common denominator of all corrosion types is a reduction in the dimensions of the corroding material. This property of corrosion will be exploited to test the proposed fiber optic corrosion sensor. The approach used to validate the ability of the proposed fiber optic corrosion sensor to measure effective dimensional changes in the metal coating material will be documented in Chapter 6.

Chapter 3 - Metal Coating Techniques

Selecting the appropriate coating technique(s) for the fabrication of the metal-clad sensors and selecting the coating material were decisions which directly impacted each other. Due to the comparatively high elastic modulus and yield strength of copper, as shown in Table 2.1, copper was selected as the coating material to be used in the experiments discussed here. An additional consideration in the selection of copper is the maturity of many copper coating techniques and the availability of copper coating material.

The prime requisite for the coating approach to be used was the need for good adhesion between the silica and copper coating. This requisite is motivated by the need for efficient stress/strain transfer across the coating/glass interface which is required to obtain accurate measurements by the EFPI gages of the strain in the coating material. A secondary requirement of the coating method is the deposition of relatively thick coatings. To be precise, using the design tables of Sirkis and Dasgupta [15], copper coating thicknesses of 40 and 80 micrometers were selected for application on the 350 micrometers outer diameter EFPI gage (the motivation for this thickness selection will be described in the following Chapter). A final consideration in the coating process selection was the availability of the equipment necessary to perform the coating processes. Balancing these three considerations, three candidate coating techniques were identified: sputtering, vacuum evaporation, electroplating. It should be noted that chemical vapor deposition (CVD) is also an attractive coating process, however, CVD facilities were not available, and therefore will not be considered for use in this thesis. However, the reader should be aware that the CVD processes are capable of producing high-yield, thick coatings, often more economically than the physical vapor deposition (PVD) processes of vacuum deposition and sputtering [16]. Overviews of the three (available) candidate techniques, sputtering, vacuum evaporation, and electroplating, are provided in the following sections.

3.1 Sputtering of Metal Coatings

Sputtering is a technique used to deposit high-quality thin coatings onto a variety of substrate materials. In the sputtering procedure, a gas plasma discharge, generally argon, is introduced between two electrodes [17]. One of the electrodes, the cathode, is the material which is to be applied. The substrate which is to be coated is attached to the other electrode, or the anode. The sputtering chamber is evacuated to a low vacuum (10^{-5} Torr), and then backfilled with the plasma gas [17]. Gas ions (positively charged) accelerate towards the cathode and strike the cathode material with a high impact which dislodges coating material atoms from the cathode. These dislodged atoms subsequently travel at high speeds to the anode attaching themselves to create a thin sputtered film.

There are a variety of different sputtering arrangements, but most require multiple cathode sources to provide even coating of the substrate material. The prime advantage of sputtering over other coating techniques is the excellent surface adhesion sputtered coatings exhibit. Unfortunately, the price of this good adhesion is an extremely poor coating deposition rate, and, due to the low vacuum required for initialization of the process, setup time for a single sputtering deposition can be up to twelve hours [18]. The deposition rate achievable with sputtering chamber is only approximately 1 micrometers/hour. Clearly, individually coating several fiber optic sensors with a 40-80 micrometers thick sputtered coating would be a time consuming endeavor.

3.2 Vacuum Evaporation Deposition of Metal Coatings

An alternative to sputtering is afforded by the vacuum evaporation coating process. The vacuum evaporation coating process is the most generalized type of coating procedure due to the wide range of coating materials which it supports, including metals, metalloids, semiconductors, and non-metals, and because it can be used to coat almost any surface [19]. All of the candidate metal coating materials identified for this research are supported by vacuum evaporation procedures. Vacuum evaporation deposition is performed in air-tight containers, typically bell jars for small yield applications. The substrate to be coated is placed in the jar and the pressure in the jar is reduced to near vacuum via a combination of both mechanical and diffusion pumps [20].

Also located in the bell jar is one (or several) tungsten filament which is the site source of the coating material. Attached to the tungsten filament is a piece of coating material stock. The tungsten filament is subsequently heated slowly via the application of an alternating current until the coating material is slightly melted and wets the source filament. Once the filament is wetted, the current to the filament is quickly increased so that the coating material rapidly evaporates. The evaporated coating material vapor molecules then isotropically disperse in the jar, coating everything in the line of sight of the source filament. The thickness of the applied coating is controlled by distance between the source and the target and the amount of coating material attached to the source, or can be directly monitored by use of a crystal thickness monitor [20]. A schematic of a evaporation chamber will be provided in the following chapter.

The surface adhesion provided by vacuum evaporation is high, although not as high as that achieved with sputtering. However, the deposition rate is considerably higher than that achieved with sputtering and the system setup time is also smaller. The key to good surface adhesion using vacuum evaporation processes is the ability to achieve a low vacuum ($\approx 10^{-5}$ Torr) in the chamber and the absence of any foreign material in the chamber, such as finger oils. The coating rate of the evaporation chamber can approach several micrometers/hour.

3.3 Electroplating of Metal Coatings

A final coating process to be considered in this thesis is electroplating. The electroplating technique to be considered here is typically performed in an aqueous, electrolytic solution. The electroplating system comprises an anode, cathode and electrolyte, or conducting solution. In contrast to sputtering, in electroplating, the cathode is the material which is to be plated. The anode is the coating material which is dissolved during the electroplating process.

In the electroplating process, as stated, the target is the cathode and the coating material is the anode; both are immersed in an electrolytic solution. In the process, the anode is connected to the negative pole of a direct current supply, and the cathode is connected to the positive pole of the current supply. The ions in the electrolytic bath are attracted to the electrodes which possess and opposite charge. Through the use of this electro-chemical cell, electroplating is achieved.

Much higher coating deposition rates can be achieved with electroplating than the two previously mentioned techniques, however, the surface adhesion afforded by electroplating processes is inferior to both sputtering and vacuum evaporation. An important part of the electroplating process is determining the amount of coating which is to be deposited. For the purposes of this research, achieving a pre-specified coating thickness is of primary interest. To accomplish this, the formulation for coating weight, W, must be examined [21],

$$W = \frac{I \cdot t}{F} \times \frac{A}{z}, \tag{3.1}$$

where I is the current used in the plating process (amperes), t is the plating time (seconds), F is the Faraday of the coating material (96,500 coulombs for copper), A is the atomic weight of the coating material, and z is the valence, or charge, of the ions released from the anode. Table 3.1 provides the relevant properties of the candidate coating material for this research. Note the absence of aluminum in Table 3.1, this is because aluminum is typically not applied as a coating material through electroplating because of the potential

Table 3.1 Important material properties for electroplating processes. (Adapted from Parthasaradhy [21])

Metal	Valency	Atomic weight	Density (g/cm^3)
Copper	1 (cyanide bath) 2 (acid bath)	63.54	8.92
Gold	1 (cyanide bath) 3 (ferrocyanide bath)	196.97	19.29
Silver	1 (all baths)	107.87	10.5

for surface oxides to form on the aluminum coated substrate thus causing poor adhesion of the subsequent layers of coating material [19]. The second important relationship in determining the coating time for a desired thickness, T, is the thickness equation, given by [21]

$$T = \frac{W}{a \times d}, \tag{3.2}$$

where a is the plated area (cm^2) and d is the density of the coating material (g/cm^3). Hence, the relationship which will provide the required coating time estimate is [21]

$$t = T(a \times d) \cdot \frac{z}{A} \cdot \frac{96{,}500}{I}. \tag{3.3}$$

As noted in Table 3.1, various baths may be used to deposit the different materials. For the work presented here, a copper acid bath was selected since a thick coating was desired. A schematic of the acid copper bath used for the electroplating process used for this research is presented in the Chapter 4.

Chapter 4 - Fabrication of Copper-Coated EFPI Sensors

For reasons discussed in Chapter 1, extrinsic Fabry-Perot interferometric (EFPI) fiber optic sensors were selected as the fiber optic sensor-type for developing the thick metal-coated post-damage inspection, corrosion, and temperature sensors. Also, due to the relatively high elastic modulus and yield strength, cost, and availability, copper was selected as the metal coating material used to construct the sensors. As discussed in Chapter 3, there is a basic trade-off in the candidate coating techniques between surface adhesion and coating deposition rate. Two coating thicknesses were selected for study in this work. Sirkis and Dasgupta [15], recommend a minimal sensor diameter/sensor plus coating diameter of 1.25 for detectable residual plastic strain levels by an interferometric fiber optic sensor. However, due to the high-sensitivity of the EFPI sensor, a lower ratio was selected for this work. Accordingly, both 40 micrometers and 80 micrometers thick coatings were chosen, providing a sensor diameter/sensor plus coating diameter ratio of 1.11 and 1.23, respectively. To apply this thick copper coating a two stage process was selected for the coating procedure consisting of the deposition of a thin layer of copper via the sputtering or vacuum evaporation techniques and subsequent over-coating using an electroplating technique.

Ten EFPI sensors were originally constructed for this research. Four of the sensors were sputtered with copper and vacuum evaporation was used to establish the base coat on the remaining six EFPI sensors. In the sputtered case, approximately 1 micrometer of copper was deposited on the sensors. Unfortunately, the sputtered coating rapidly oxidized once introduced to the environment which rendered the sensors unusable for the electroplating process because good electrical contact to the sensors could not be established.

Since the sputtered sensors were unusable for this research, a description of their fabrication will be omitted from discussions of the sensor fabrication procedures. Accordingly, only the vacuum evaporation and electroplating fabrication steps will be documented. This chapter describes the fabrication process for the metal-coated EFPI sensors used in this research. The Section 4.1 describes the fabrication process of the EFPI sensors. Section 4.2 overviews the evaporation procedure used to produce the thin copper undercoating on the EFPI sensors and Section 4.3 describes the electroplating process used to apply the remaining copper coating to achieve the desired thick copper coating on the sensors.

4.1 EFPI Fabrication

Ten EFPI sensors were constructed as shown in Figure 4.1. The EFPI sensors were fabricated by inserting two single mode, polyimide coated optical fibers into a polyimide coated silica capillary tube. High-temperature adhesive was then used to affix the two fibers within the tube; the adhesive used to fabricate the sensors used for this research was Miller-Stephenson 907 (MS-907). The MS-907 is subsequently thermally cured at 100°C for 20 minutes.

As stated in Chapter 1, the distance between the two adhesive points define the gage length of the sensor and the distance between the two fiber endfaces is termed the gap separation; the target gage and gap distances for the sensors were 1 centimeter and 50 micrometer, respectively. The actual gage lengths of each sensor is provided in

Chapter 5. The final step in the EFPI sensor fabrication procedure was to remove the polyimide coating on the capillary tube and the input/output and reflector fibers in the vicinity of the capillary tube. The removal of the polyimide coating was deemed appropriate so that maximal adhesion could be achieved at the sensor/coating interface [20]. The coating was removed via fusion splicing in which a high arc current is applied across the sensor and effectively burns off the coating material.

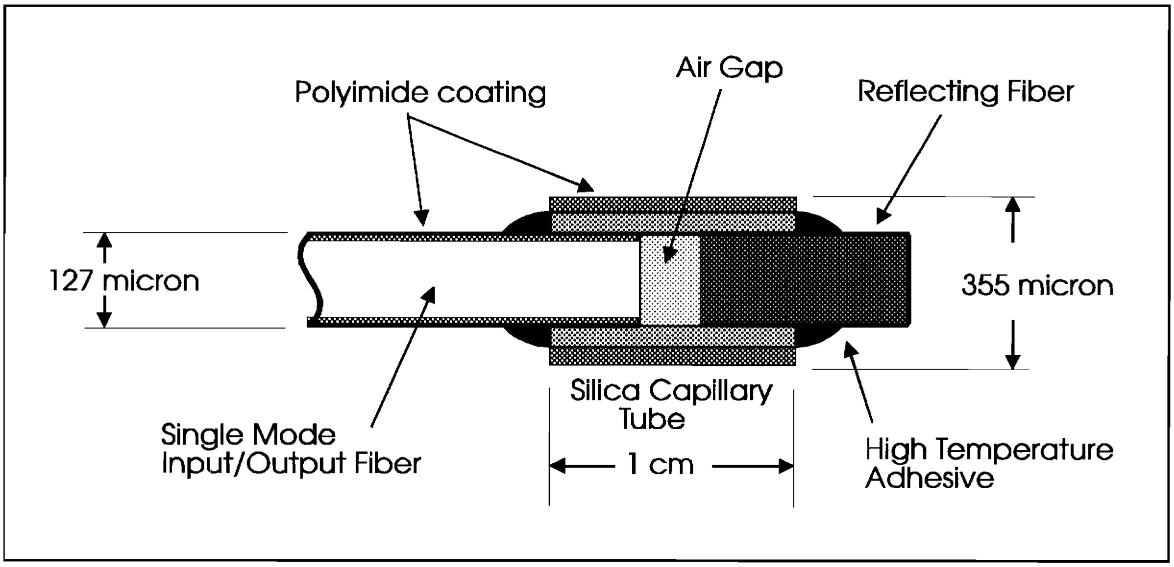

Figure 4.1. Diagram of EFPI sensor head used for construction of metal-coated sensors.

4.2 Vacuum Evaporation Procedure

The first step in the EFPI coating process was to apply a thin copper coating to the sensors via vacuum evaporation. The vacuum evaporation process encourages high adhesion between the coating material and silica sensor surface. Prior to the evaporation process, the surface of the sensor was cleaned in a two-step process in which the sensor was first dipped in an acetone bath. To remove any residue deposited on the sensor surface by the acetone bath, the sensor was then cleaned with de-ionized water. Figure 4.2 shows the vacuum evaporation setup used to coat the sensors. As shown in

Figure 4.2, a frame was constructed to hold the EFPI sensors during the coating process which could be rotated during the deposition.

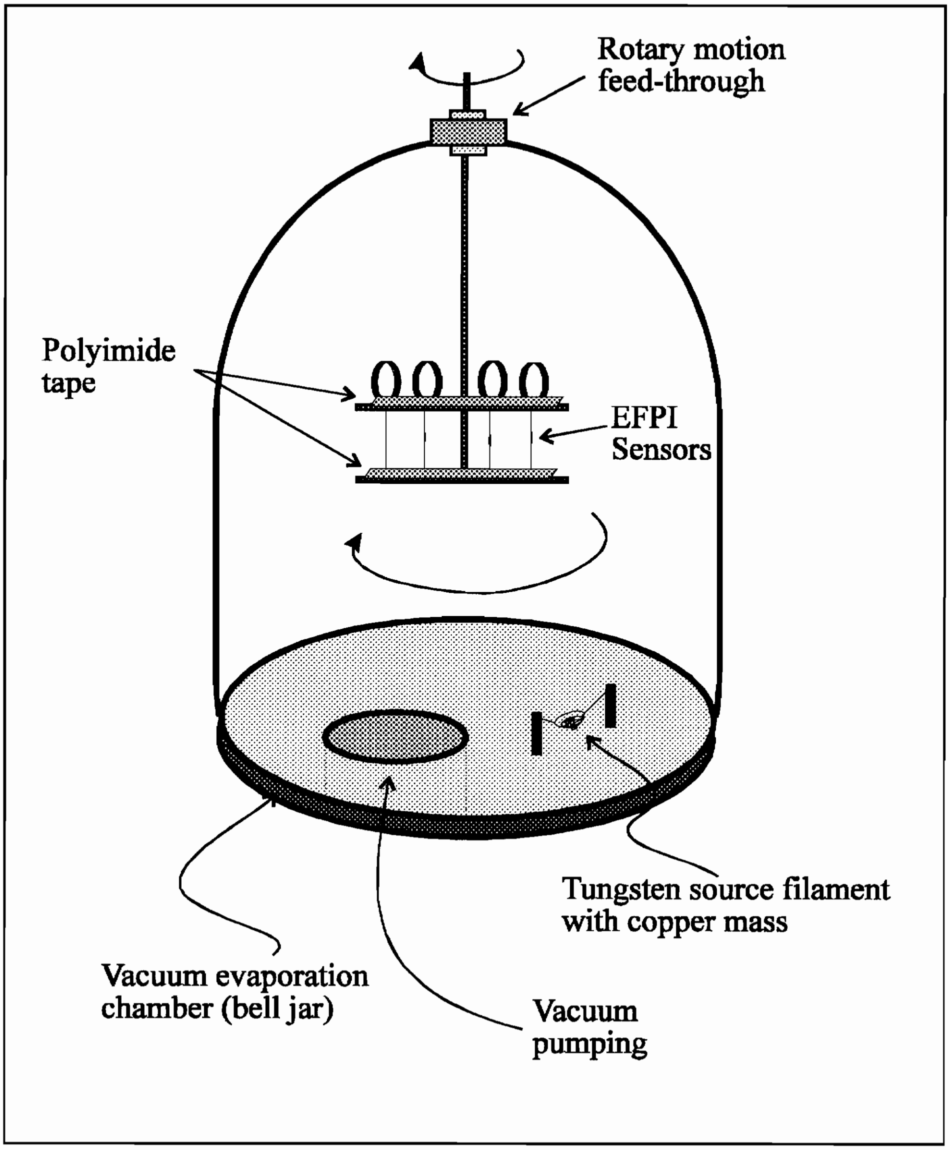

Figure 4.2. Schematic of vacuum evaporation equipment used for base coat application on the EFPI sensors.

As stated in the Chapter 3, vacuum evaporation is a line-of-sight type coating process and therefore rotation of the sensors during the coating process was required to insure the application of a uniform coating thickness. A single tungsten filament source site was used to heat the copper coating material which was approximately 99% pure copper. During the evaporation process, a copper coating of several micrometers was applied to the sensors. The exact thickness of the evaporated copper coatings was unimportant since subsequent recoating via electroplating was to be performed. Section 4.3 documents the electroplating process used to deposit the remaining thickness of copper on the sensor elements.

4.3 Electroplating Procedure

The final step in the coating process was electroplating. The electroplating process utilized the thin copper coating deposited by the vacuum evaporation procedure to establish the necessary cathodic site for the coating to be deposited upon. The properties of the electrolytic solution (acid copper bath) used for the electroplating process are provided in Table 4.1. Figure 4.3 shows the setup used to perform the electroplating. As shown in Figure 4.3, two copper electrodes were used as the anodes in the electro-chemical circuit. An aerator was used to "stir" the electrolytic solution during the coating process.

Prior to the plating process, the outer diameter of each sensor was measured using a micrometer which provided a measurement resolution of 0.1 micrometers. Once the diameter of each sensor was found, the surface area to be coated was calculated and used in equation 3.3 to determine the time required to achieve the desired coating thickness. A current of 30 amperes/foot^2 was selected for use during the coating process. At this current, a deposition rate of 20 micrometers/hour was achieved.

Table 4.1. Recipe for acid copper plating solution (electrolytic).

Acid Copper Bath (80°F)	
component	amount
$CuSO_4$	240 grams/liter
H_2SO_4	15 grams/liter
Cl^-	100 ppm
Thiourea	0.001 grams/liter
wetting agent (Ivory dishwashing liquid)	0.1 grams/liter
brightner	1 milliliter/liter

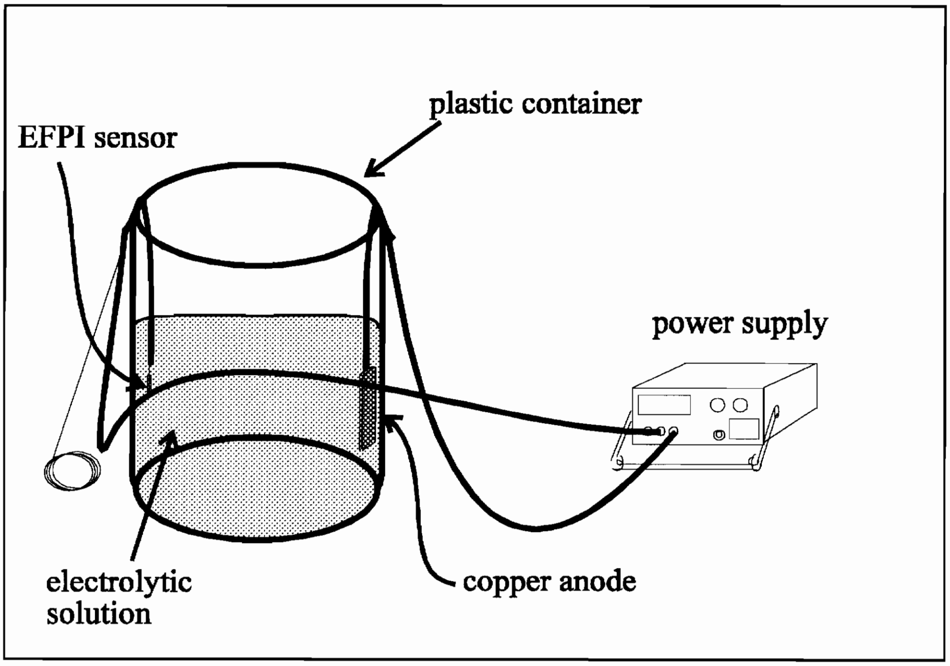

Figure 4.3. Setup used for electroplating procedure.

As previously mentioned, three sensors were coated to a thickness of 40 micrometers and three sensors were coated to a final thickness of 80 micrometers. After the plating process, the outer diameter of each sensor was measured, and errors on the order of ±3 micrometers were observed. For the purposes of this research, this was deemed to lie within an acceptable coating thickness error tolerance. Chapters 5-8 document the application of the metal-coated sensors to post-damage inspection, corrosion, and temperature sensing applications, respectively.

Chapter 5 - Metal-Coated EFPI Sensors for Post-Damage Inspection Applications

Of particular interest to the non-destructive evaluation of materials is the ability of a sensor to measure residual strains within a material specimen which may at some point compromise the structural integrity of the specimen. The ability of the EFPI to detect residual strains was demonstrated by Poland et al. [22] in the measurement of residual strains in a composite material specimen resulting from a high-energy ballistic impact on the specimen. Jones et al. further demonstrated the ability of the EFPI sensor to characterize residual strains by measuring the hysterisis of a concrete specimen subjected to cyclical loading [23].

The demonstrated ability of the EFPI to measure residual strains may be exploited to create a post-damage inspection measurement device. In the post-damage inspection application, the EFPI sensor is coated with an elastic-plastic material, such as a ductile metal. Once the coated sensor is thermally or mechanically strained, the plastic properties of the coating material causes the coating to retain residual strains [15]. Sirkis and Dasgupta [15] present and in-depth analysis of the theoretical phase-strain relationship in a thick metal-coated fiber optic sensor. Further development of the theory developed by Sirkis and Dasgupta is beyond the scope of this research effort, however, the key result of the work by Sirkis and Dasgupta is that the residual strain induced in a thick metal-coated fiber optic sensor is a function of coating material, coating thickness, and the loading history of the sensor.

The primary thrust of the post-damage detection sensor developed here was to establish an empirical relationship between residual strain measured by the EFPI sensor for a given peak strain level, coating thickness and coating material. As previously discussed, copper was chosen as the coating material for this study due to the high ductility of copper, low cost, and considerations of the available coating techniques. Depending on the application and environment, gold, silver, aluminum and nickel, are other coating material candidates which could have been used [15,24].

5.1 Post-Damage Inspection Sensor Experimental Setup

For the sensor characterization work presented here, the zero-stress reloading approach, discussed in Section 2.1.1, was selected. In zero-stress reloading, a material is strained, allowed to relax with zero applied stress, and then reloaded via straining. An alternative approach which could have been taken for the investigation would be the zero-strain reloading approach. Zero-strain reloading is described by straining a material specimen, applying a stress opposite to the original stress until the material specimen regains the original length, and subsequently reloading the specimen. For real-world applications of the post-damage inspection sensor, both situations could be encountered; this issue will be addressed further in Chapter 8.

An attractive benefit of using the zero-stress reloading approach is that it provides a method to directly evaluate whether the elastic, linear hardening model is an appropriate choice to describe the sensor. Recalling from Chapter 2, the elastic, linear hardening model implies that the stress/strain relationship after yield of a material specimen is linear and that the slope of the stress/strain relationship after stress removal always possesses negative slope of the elastic modulus of the material. The elastic, linear hardening model further implies that the residual strain versus peak applied strain is linear (see Figure 2.3), thus yielding a convenient way to validate choice of the appropriate rheological model. If the residual strain versus peak applied strain relationship was not linear, then the yield strength of the material would be a function of the loading history of the sensor and a elastic, non-linear hardening model would be needed.

A testing approach could have been developed to retain a sizable length of the reflecting fiber of the EFPI sensor so the sensor could be easily wrapped around mandrels in a axial load frame and subsequently testing the sensors by loading them to preselected tensile forces which would have allowed direct construction of the stress/strain relationship for the metal-coated coated sensor element. However, as mentioned in Section 4.1, to facilitate good surface adhesion of the metal to the sensor, the polyimide coating from the sensor and surrounding fiber was removed. From previous experience, such a removal of the polyimide overcoating seriously compromises the tensile strength of an EFPI and therefore an alternative testing procedure was selected. Future work on the post-damage inspection sensor could be to identify coating processes which support direct application of the metal on the polyimide optical fiber overcoating.

A schematic of the selected experimental setup is shown in Figure 5.1 As shown, a micro-positioner was mounted to a metal block. At one end of the metal block, an acrylic slab was attached to the block which had the same approximate height as the positioner surface. The key to using the technique shown in Figure 5.1 was that each sensor had to be strained, and then released, so that the residual strains maintained in the coated sensor element could be measured. The zero-stress reloading approach was realized by using phenolsalicylate as a sensor attachment medium. Phenolsalicylate comes in a crystalline form, but liquefies at temperatures slightly above room temperature. Additionally, acetone is an excellent solvent for phenolsalicylate; in fact, phenolsalicylate dissolves almost instantly on contact with acetone.

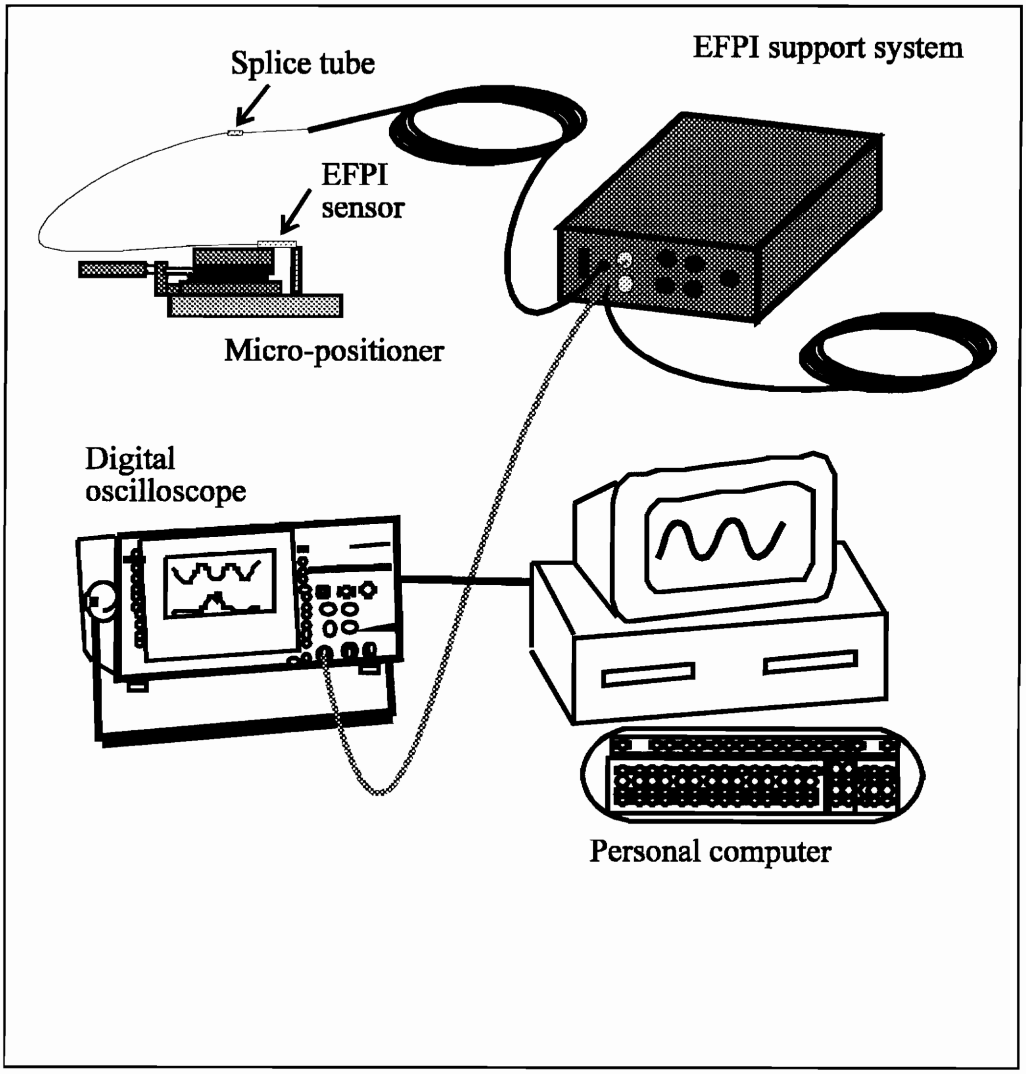

Figure 5.1 Experimental setup used in post-damage inspection sensor testing.

As shown in Figure 5.1, one end of the sensors was attached to the acrylic block and one end of the sensors was attached to the surface of the positioner. The sensors were attached so that the axial direction of the sensors was the same direction as the translation axis of the positioner. The sensor lead-in/out was connected to an EFPI support system which housed the source and detector components for operating the sensors. The output of the EFPI support system provides an output voltage signal proportional to the intensity of the optical signal received by the photodetector (see Figure 1.1). The output signal from the EFPI support system was fed via a coaxial cable to a digital storage oscilloscope which provided the function as an analog-to-digital (A/D) converter and data storage device. After capturing the event on the digital oscilloscope, the data was downloaded in ASCII format to a personal computer for processing and evaluation. As mentioned in Section 4.1, four of the original ten sensors did not survive the coating process. Unfortunately, one of the remaining six sensors lacked proper adhesion between the coating material and silica sensor surface and was discarded. Hence, a balance of only five sensors remained for the experiments, two with a 40 micrometer thick copper coating and three with a 80 micrometer thick copper coating. The important information regarding the 5 test sensors is provided in Table 5.1. The need for a larger sample size of sensors is recognized, however, due to the high cost associated with the fabrication of the sensor elements, the fabrication of additional sensor elements was not possible for this research.

The testing of the sensors was performed in consistent manner although each sensor was tested independently due to the limited availability of support electronic systems. In the testing, each sensor was displaced in approximate steps of 2 micrometers over the sensors gage length. For example, a sensor was attached, and displaced approximately 2 micrometers while the response of the sensor was recorded on the digital storage oscilloscope. The phenolsalicylate on the acrylic block was then dissolved, and the output of the sensor system during relaxation of the sensor element was again recorded. The sensor was then re-attached to the acrylic block and displaced approximately 4 micrometers while the sensor output was recorded. The phenolsalicylate on the acrylic block was again dissolved, and the relaxation of the sensor element was again recorded; this process was repeated until the phenolsalicylate used for the attachment failed during a displacement event which typically occurred at a displacement of 12-14 micrometers. It would have been desirable to subject the sensors to a higher peak displacement (load), but availability of materials and equipment prevented this from being achieved. Future work could be tailored to use a load frame which could impart higher loads to the sensor elements and explore the full range of residual coating strains up to mechanical failure of the sensor elements.

Table 5.1 Coating thicknesses and gage lengths of the post-damage inspection sensors.

Sensor #	Coating Thickness	Gage Length
1	40 micrometers	10.10 millimeters
2	40 micrometers	10.10 millimeters
3	80 micrometers	10.20 millimeters
4	80 micrometers	10.15 millimeters
5	80 micrometers	10.20 millimeters

5.2 Post-Damage Inspection Sensor Test Results

Figure 5.2 shows typical time-series data of the post-damage inspection sensor responses. Figure 5.2(a) presents the entire event, including both the straining and relaxing of the coated sensor element. Figure 5.2(b) shows a expanded view of the displacement event;

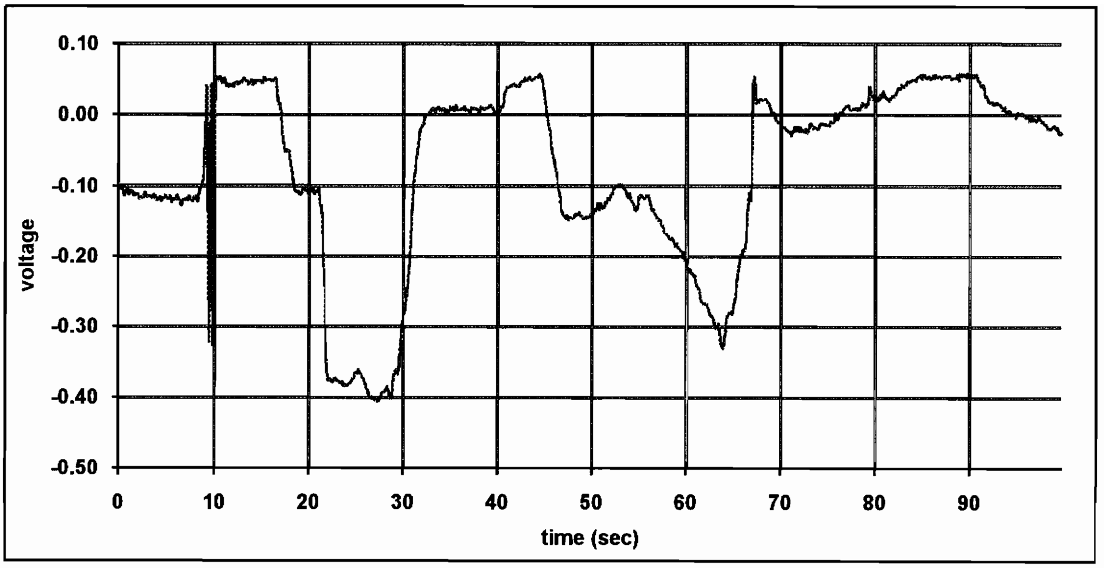

(a)

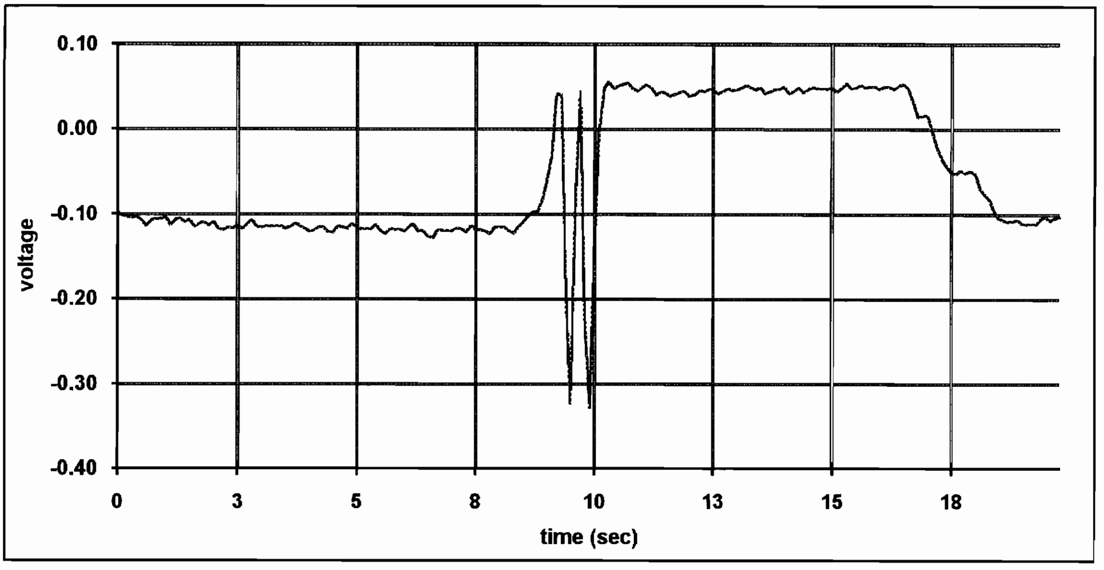

(b)

Figure 5.2. Typical sensor data from the post-damage inspection sensor experiments; (a) plot of entire event, (b) expanded view of t=0 to t=20 seconds in (a).

note in Figure 5.2(b) the almost classical interference fringes obtained by the sensor. The data shown in Figure 5.2 is for the first 2 micrometer event for sensor 3. Note the small residual strain evident in the plot which is demonstrated by the difference in the beginning and ending voltage levels of the sensor's output. Also note the relatively rapid displacement imparted to the sensor, but the gradual strain relaxation as the phenolsalicylate fully dissolved.

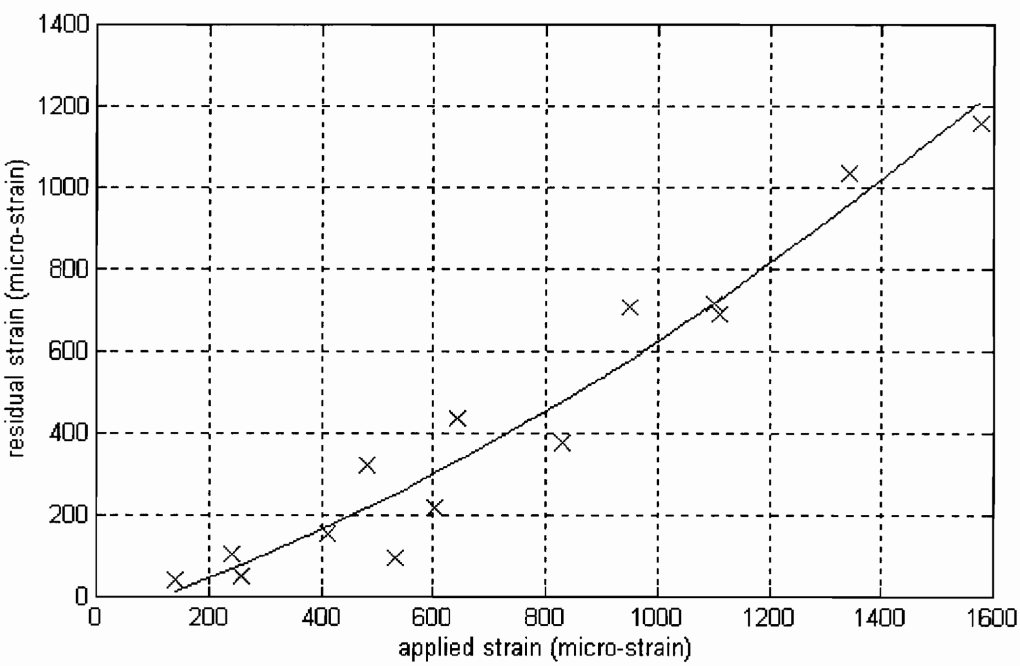

Figure 5.3. Results from post-damage inspection sensor experiments for EFPI sensors coated with 40 micrometer thick copper coating with least-squares fit to data.

Figure 5.3 presents the results of the experiments conducted with the sensors possessing the 40 micrometers thick copper coating. An *x* is used to mark the observed data points and the line is the least-squares fit to the data. Note that according to the least-squares fit, residual strain was first measured with a peak induced strain of approximately 150 microstrain which indicates that the yield stress of the coated sensor is achieved at this peak strain level and that application of strain exceeding this level will induce plastic deformation of the sensor element.

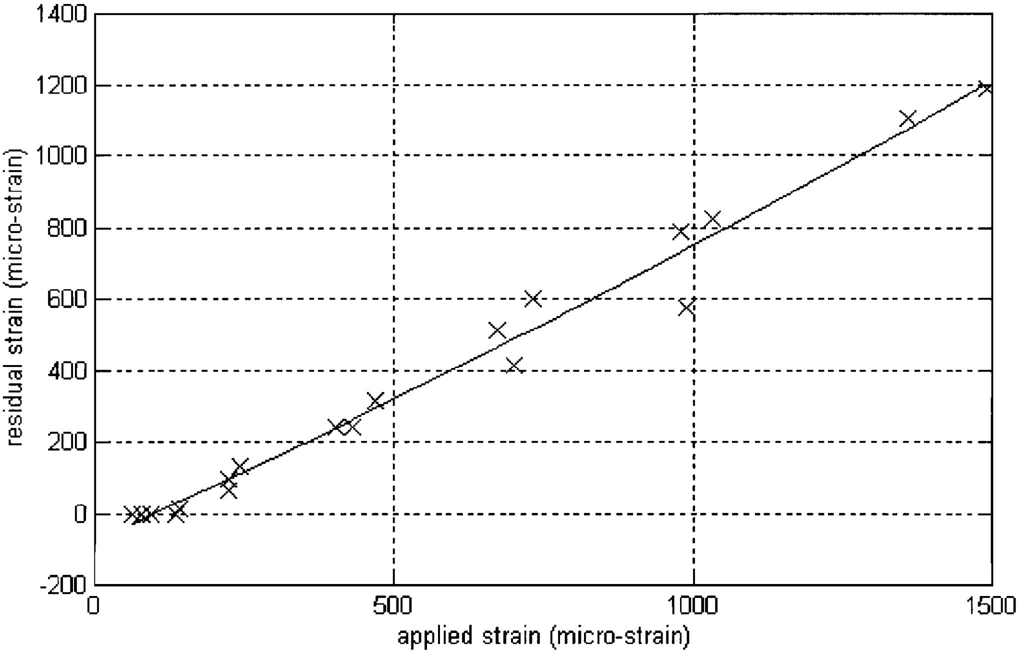

Figure 5.4. Results from post-damage inspection sensor experiments for EFPI sensors coated with 80 micrometer thick copper coating with least-squares fit to data.

Figure 5.4 presents the experimental results obtained using the 80 micrometer thick copper coated sensors. Again note the minimum detectable residual strain in the neighborhood of an applied 150 microstrain peak strain which again indicates the peak strain corresponding to the yield strength of the sensor. Also note the similarity in shape of the least-squares fits in Figures 5.3 and 5.4, however, the grouping of the data for the 80 micrometer coating thickness is superior to the results obtained with the 40 micrometer coated sensor which is possibly explained by the deviation of the actual coating thicknesses from the desired thicknesses, i.e., the observed ± 2 micrometer coating thickness error due the coating process would have less impact on the 80 micrometer thick coated sensor than the 40 micrometer thick coated sensor.

Figure 5.5 provides a comparison of the least-squares fit to the data for the two coating thicknesses which indicates that, as expected, the sensor with the thicker coating registers the larger residual strain, and at no point do the two design curves intersect each other. Also note in Figure 5.5 how both of the curves cross the zero residual strain axis at approximately the same point which is not surprising considering the modeling performed by Sirkis and Dasgupta [15] who provide design curves for the thick copper-coated sensors relating coating thickness to peak strain. The modeling performed by Sirkis and Dasgupta shows that for the coating thicknesses used here, low peak strain levels will result in similar residual strain levels since the yield strengths of the two sensors will be very similar. As the coating thicknesses become more dissimilar (coating thicknesses differ on the order of several sensor diameters), a greater differential in residual strain for a given peak strain will result; this property facilitates the use of the post-damage inspection sensor as a threshold detector.

Probably the most important observation which can be made about Figure 5.5 is that the peak strain vs. residual strain relationship for the 40 micrometer thick coated sensor possesses a curvature whereas the relationship is approximately linear for the 80 micrometer thick coated sensor. As discussed in Section 2.1, a linear peak strain versus residual strain relationship indicates an elastic, linear hardening type system which indicates that *the sensor with the 80 micrometer thick copper coating closely obeys the elastic, linear hardening model*. Additionally, although the results are not conclusive, Figure 5.5 indicates *the elastic, non-linear hardening model is required to describe the metal-coated sensor with the 40 micrometer thick copper coating*. From a practical standpoint, the linear peak strain versus residual strain relationship of the thicker-coated sensor indicates that the 80 micrometer coated sensor is preferred as compared to the 40 micrometer coated sensor since the mechanical loading response of the thicker coated sensor can be described by the simple elastic, linear hardening model.

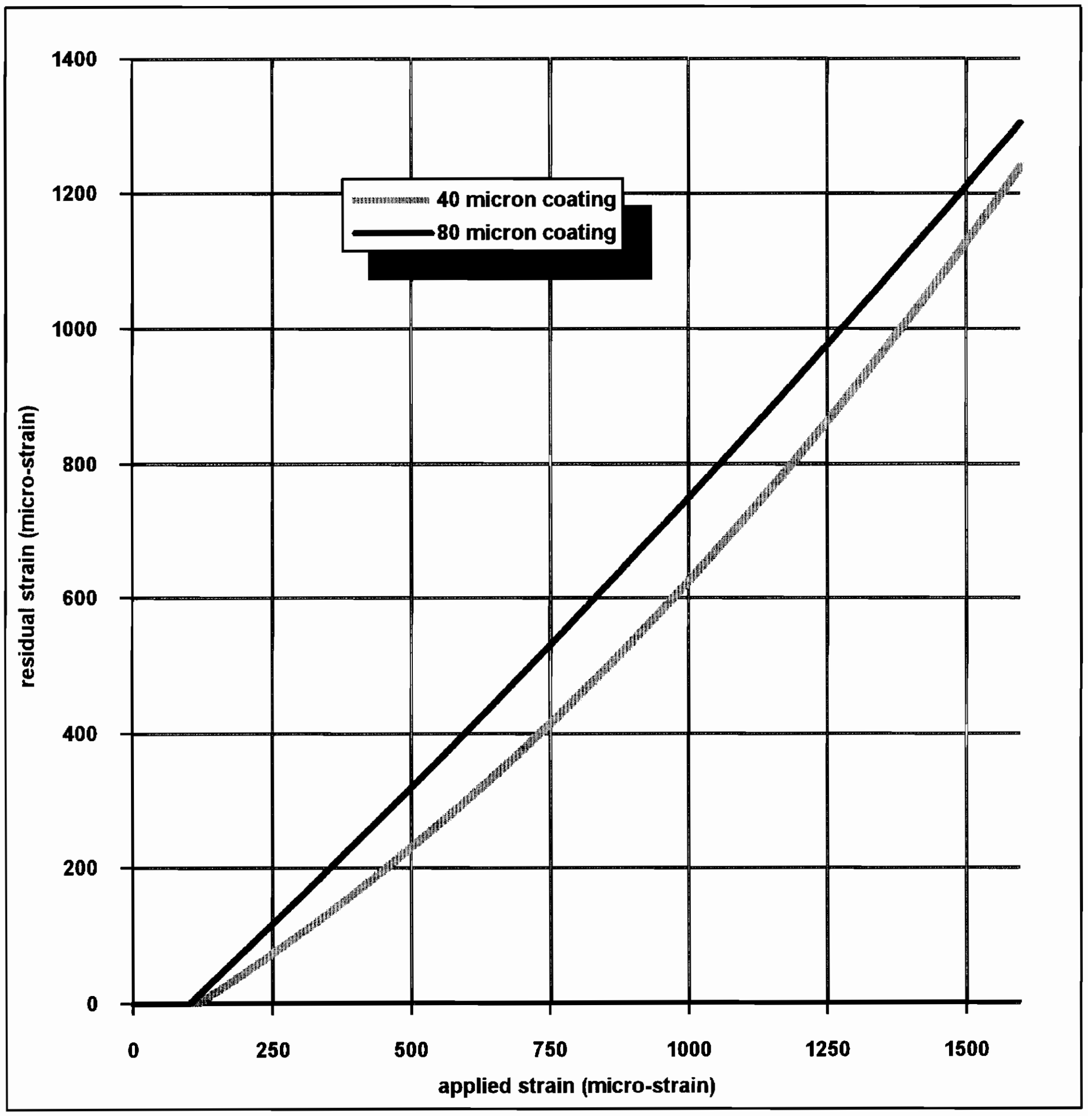

Figure 5.5. Least-squares fit to post-damage inspection sensor data for EFPI sensors with 40 micrometer and 80 micrometer copper coatings.

Chapter 6 - Corrosion Sensing Technique Using Metal-Coated EFPI Sensors

By exploiting the demonstrated ability of the EFPI to measure residual strains, an EFPI-based corrosion sensor will be demonstrated which is based on the post-damage inspection sensor described in Chapter 5. Prior to implementation, the corrsion sensor is to be mechanically strained until the plastic properties of the coating material cause the coating to retain residual strains. Pre-straining of the sensor will serve as the basis for the proposed EFPI-based corrosion sensor.

In Chapter 5 it was shown that the magnitude of residual strains in the EFPI copper coating induced by (pre-) straining the sensor are primarily a function of the coating material, coating material thickness and the load history of the sensor. Note that for the technique which is presented in this thesis, the coating material and thickness are controlled during the fabrication of the sensor and the load history is simply the controlled pre-straining event; hence, if any of these three sensor parameters change, specifically coating thickness, the residual strain induced on the sensor by the coating will.

The dependence of the measured residual strain on coating thickness is the basis of the corrosion sensor. As the environment attacks the surface of the metal-clad sensor, the resulting electrochemical reaction will create a corrosion cell with the sensor serving as the anode in the cell. Accordingly, as the metal particles flow from the sensor head into the environment (electrolyte), the mass of the corroding sensor coating will decrease causing an effective reduction in the coating thickness. Since the coating material (with the exception of the oxidation layer on its surface) and the load history of the coated sensor remain constant throughout the corrosion process, a reduction in the residual strains being measured by the sensor will occur as the coating thickness is effectively decreased due to the corrosion process. The life-cycle of such an EFPI-based corrosion sensor is shown in Figure 6.1. For the experiments presented in this thesis, an accelerated chemical corrosion process will be used in place of the previously described electrochemical process for reasons discussed in Section 2.2.

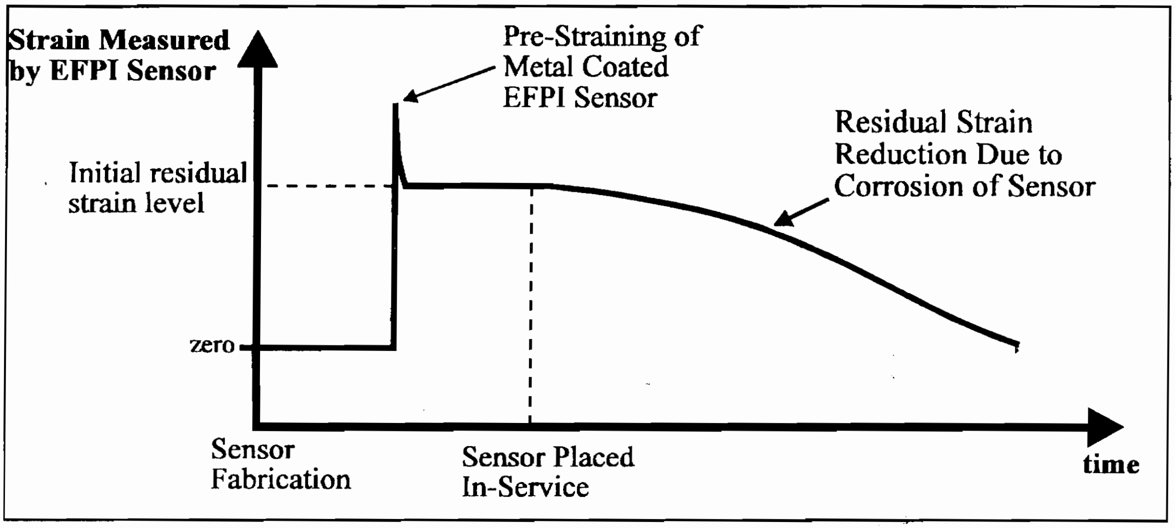

Figure 6.1 Life-cycle of EFPI-based corrosion sensor.

6.1 EFPI-Based Corrosion Sensor Experimental Setup

For the corrosion sensor experiments, sensors 1-4 in Table 5.1 were reserved for corrosion testing. Unfortunately, sensor 1 was damaged prior to the corrosion experiment and the corrosion data for sensor 2 was lost due to a data acquisition error. Figure 6.2 shows the experimental setup for the corrosion experiments. As shown, the sensors were immersed in a bath of nitric acid while monitored by an EFPI support system. As in the post-damage inspection sensing experiments, the output of the EFPI support sytem was digitally sampled and stored on a digital storage oscilloscope and subsequently downloaded to a personal computer for processing and evaluation.

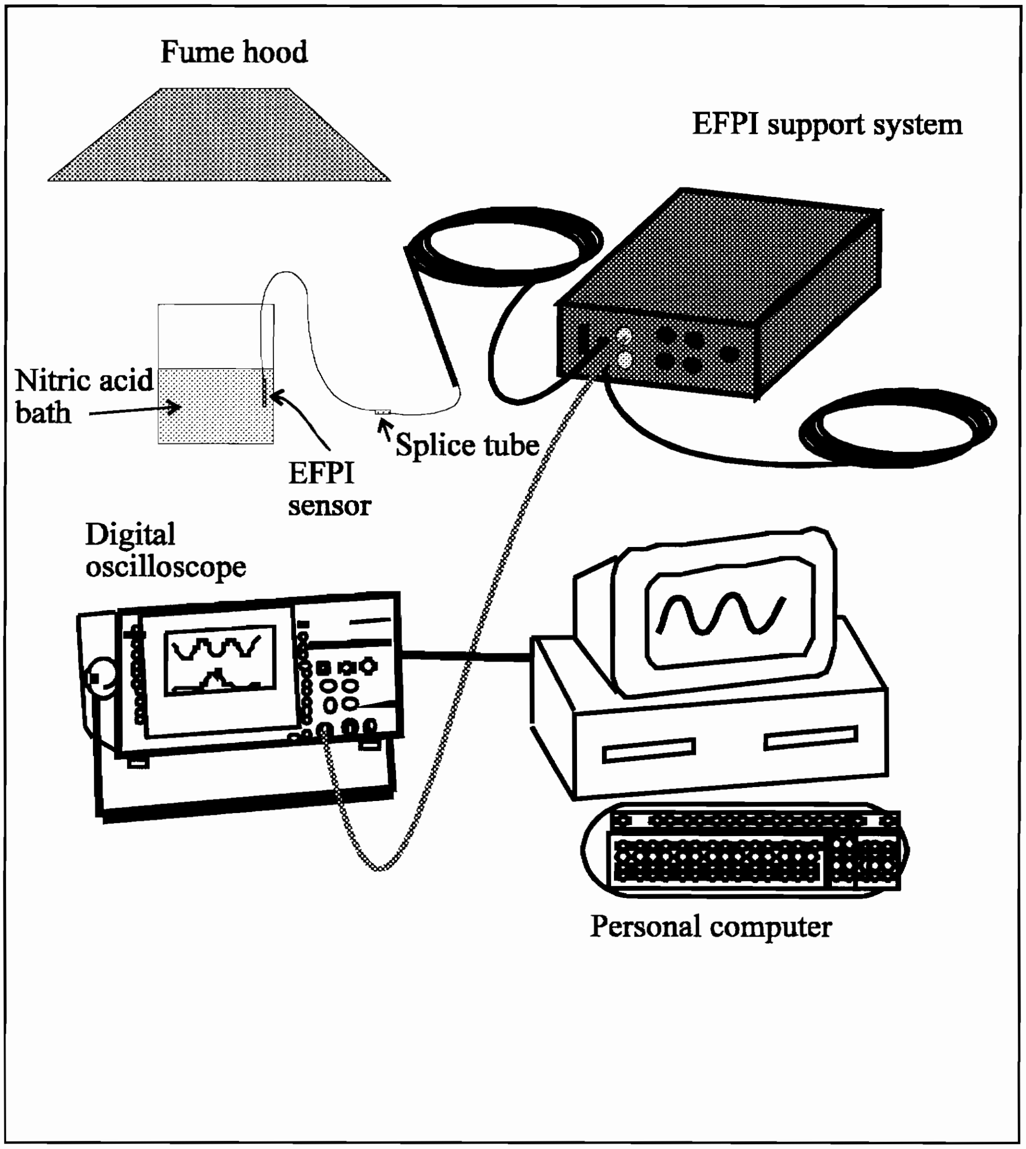

Figure 6.2. Test setup for corrosion sensing experiments.

Although the corrosion experiments conducted for this research were not conducted under an accepted corrosion testing procedure, the primary purpose of the experiment was to prove the concept of the sensor type. Nitric acid is a common chemical used in accelerated corrosion testing, but typically nitric acid vapors are used to induce the corrosion.

6.2 EFPI-Based Corrosion Sensor Test Results

As stated in the introduction of this chapter, the goal of this experiment was to measure the change in strain state of the (pre-strained) metal coated EFPI sensor as the nitric acid corroded the coating material, effectively reducing the thickness of the coating. The sensors tested in the post-damage inspection experiments were used for these corrosion experiments since the residual strains reported by the sensors during the straining events had been carefully recorded. Figure 6.3 shows a typical sensor output obtained during the corrosion experiment (sensor 3). Figure 6.3(a) presents data from the entire corrosion event, while Figure 6.3(b) provides an expanded view of the rapid relaxation of the residual strain experienced by the sensor when the sensor was first introduced to the nitric acid bath.

Figures 6.4 and 6.5 show the linearized sensor output for the corrosion experiments (sensors 3 and 4). Note in Figures 6.4 and 6.5 the rapid decrease in residual strain at the onset of the event (as indicated in Figure 6.3), and the gradual decay of the residual strain thereafter until all of the coating material had been removed by the nitric acid. The starting point in the plot in Figures 6.4 and 6.5 is the residual strain measured by the respective sensors in the post-damage inspection experiments. Although residual strain relaxation induced by the corrosion experiment does not exactly equal the value of the measured residual strain, the strain relaxation reported by sensor 4, shown in Figure 6.4, is

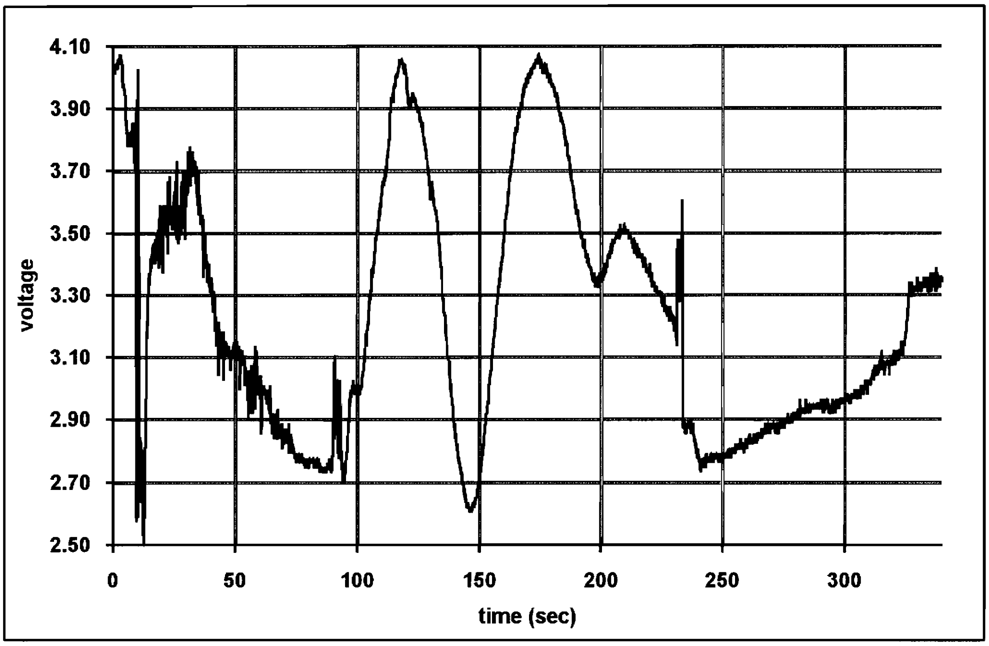

(a)

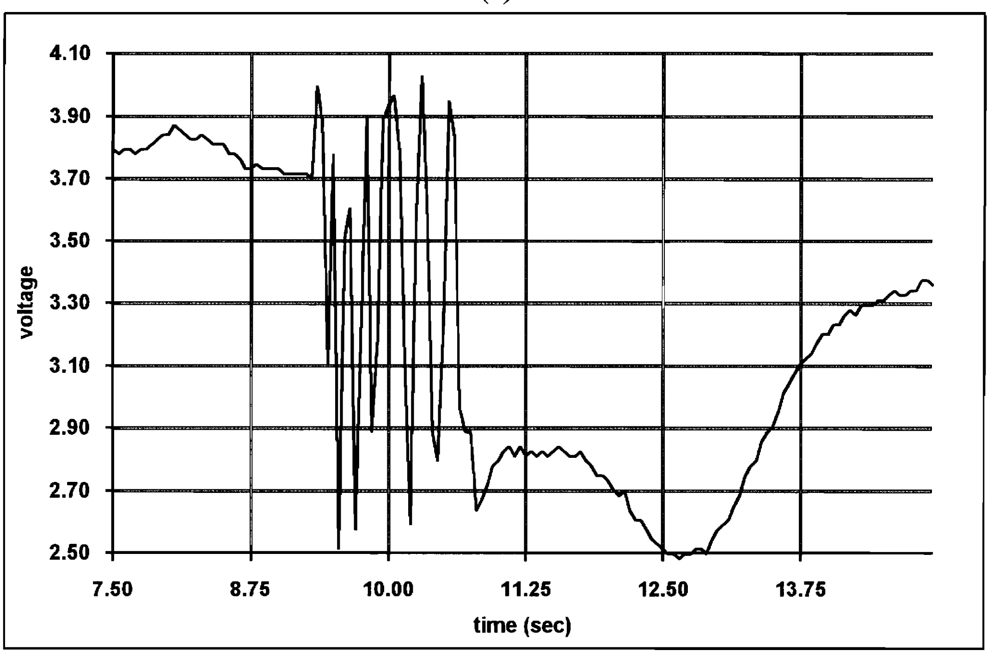

(b)

Figure 6.3. Typical sensor output during corrosion experiments (a) plot of entire event, (b) expanded view of t=7.5 seconds to t=15 seconds in (a).

only 8 % less the residual strain measured in the post-damage inspection experiments described in Chapter 5 for the same sensor. Figure 6.5 indicates that sensor 3 only showed a 1 % deviation between the previously recorded residual strain state of the sensor and the strain relaxation measured during the corrosion experiment. Due to the low errors shown in these results, it is believed that these discrepancies can be primarily attributed to experimental error. A possible explanation for this error is different environmental temperatures at the post-damage inspection sensor test location and the corrosion test location.

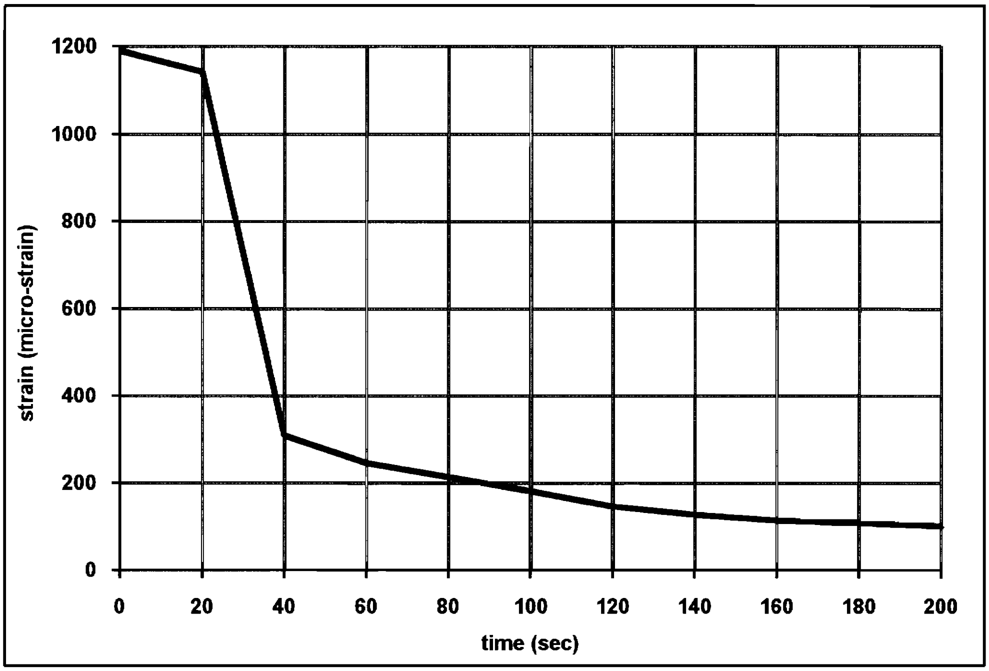

Figure 6.4. Time series strain data of corrosion experiment for 80 micrometer thick copper coated EFPI sensor (sensor 7).

Although the two sensor limitation in these corrosion experiments prevents any sound statistical interpretation of the results, it should be noted that the mean error in the two experiments was only approximately 4.5 %, which clearly indicates that further investigation of this corrosion sensing technique is warranted. Future work should be conducted with metal-clad sensors that have been more carefully pre-strained via the guidelines discussed in Chapter 5 and the corrosion environment should be more carefully controlled during the performance of the tests. A final important observation which should be explored in Figures 6.3 and 6.4 is the rapid strain reduction at the onset of the experiments. This rapid strain relaxation could be due to the larger coating surface area present at the onset of the experiment. Although the surface area consideration likely had some impact on the results, a more important potential explanation is not as obvious.

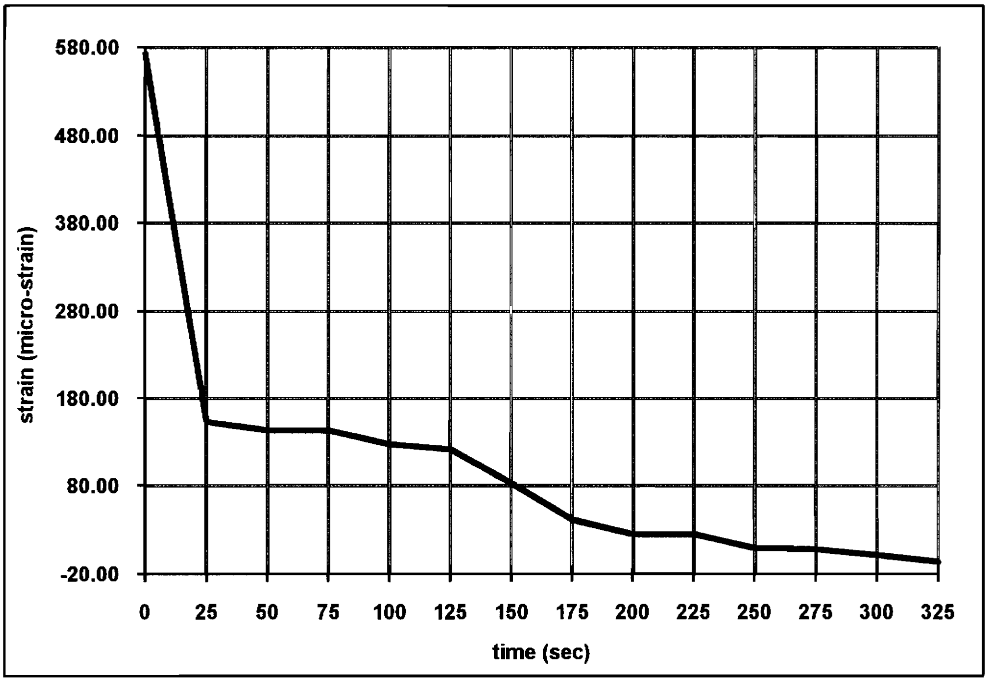

Figure 6.5. Time series strain data of corrosion experiment with 80 micrometer thick copper coated EFPI sensor (sensor 6).

A second explanation for the rapid strain relaxation at the onset of the experiements is that the residual axial strains in the coating material are not uniformly distributed throughout the coating. Intuitively, a non-uniform residual strain distribution in the coating material seems possible, since, with respect to the highly ductile coating material, the silica sensor can be considered elastic [15]. In Chapter 3 it was stated that, to promote the efficient transfer stresses across the boundary coating/glass interface, an important requisite for proper operation of the metal-clad sensors is good surface adhesion at the coating/glass interface of the sensor. If the silica sensor is considered elastic and the stress/strain boundary conditions are actually continuous, it would then be expected that higher plastic strains would occur near the surface of the coating assembly. This non-uniform strain distribution in the coating material is an important area which needs further analysis during future development of the fiber optic corrosion sensor.

As mentioned earlier in this chapter, a potential source of error in the corrosion sensing experiments is temperature effects. In Chapter 7, the thermal-apparent strain properties of the metal-clad sensors will be explored.

Chapter 7 - Temperature Sensing Using Metal-Coated EFPI Sensors

The metal-coated fiber optic sensors thus far discussed also have good temperature sensing properties due to the high coefficient of thermal expansion of copper (α = 16.74 microstrain/°C). A consequence of this property of the sensor is the deleterious effects these thermal characteristics may have on the performance of the post-damage inspection and corrosion sensors thus far discussed. Hence, the purpose of this Chapter is two-fold:

- to demonstrate the temperature sensing capabilities of thick metal-coated EFPIs, and
- to preliminarily characterize the thermal-apparent strain properties of the thick metal-coated sensor for post-damage inspection and corrosion sensing applications.

Section 7.1 documents the experimental setup for this stage of the research and Section 7.2 evaluates the sensitivity of the sensor to temperature.

7.1 Temperature Sensing Experimental Setup

Figure 7.1 presents the experimental setup used for the temperature sensing experiment. As shown, the sensor was placed on a hot-plate next to a thermocouple with a digital readout. The sensor was connected to an EFPI support system which was in turn connected to a digital oscilloscope for data acquisition and storage. After the experiment, the data stored in the digital oscilloscope was downloaded to a personal computer for processing.

For the temperature sensing experiment, the temperature of the hot-plate was raised to 70°C prior to the experiment. The temperature of the hot-plate was then ramped to an

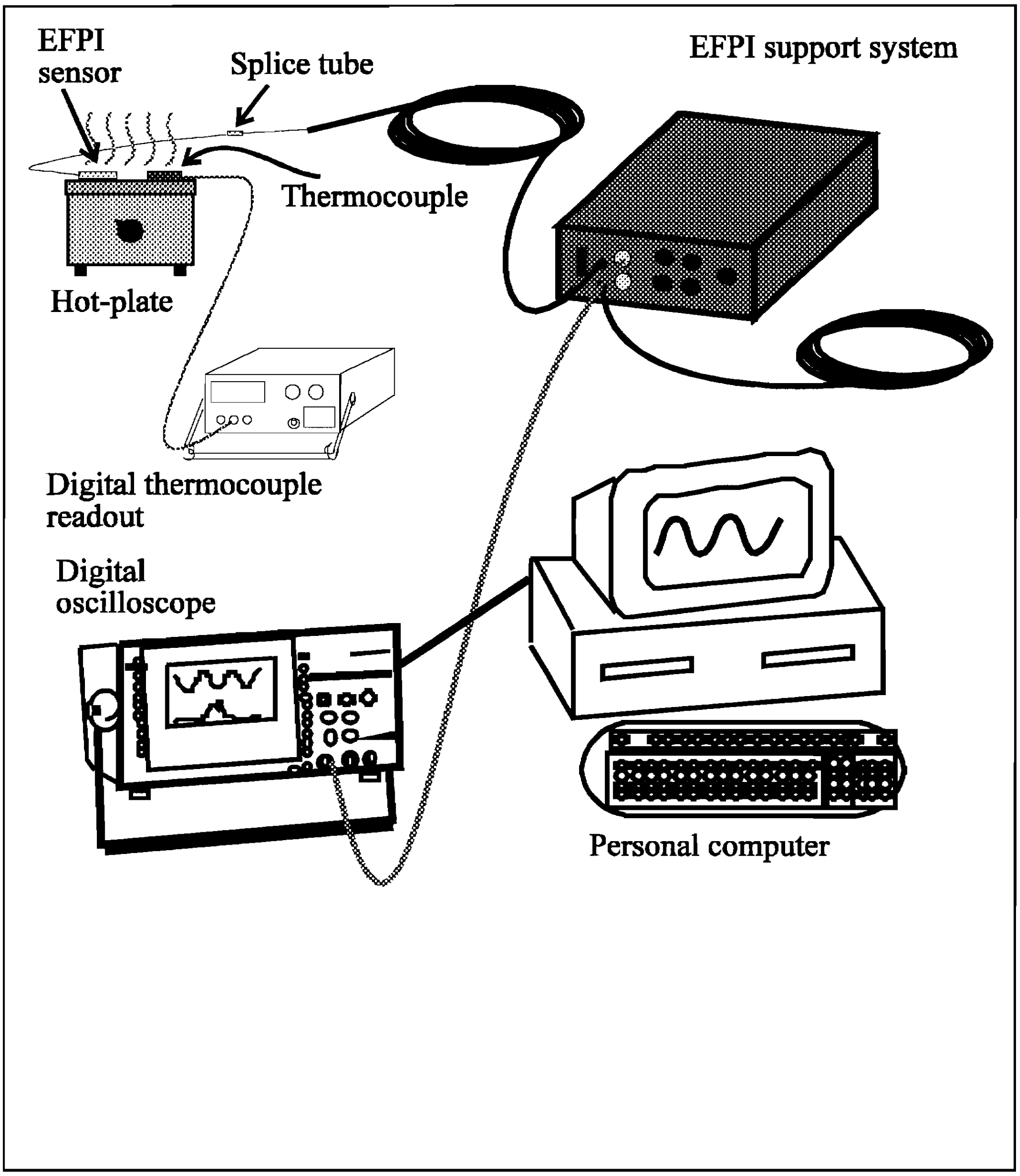

Figure 7.1. Experimental setup for temperature sensing experiment.

approximate temperature of 170°C (161 °C). The output of the sensor was recorded by the digital oscilloscope and temperature readings were manually taken from the thermocouple every 50 seconds. During the data reduction procedure of the sensor data, strain reported from the sensor was synchronized in time with the manually recorded temperature data.

7.2 Temperature Sensor Test Results

Figure 7.2 presents the results of the temperature sensing experiment. Plotted in Figure 7.2 is the time-series strain reported by the sensor, with individual data points marked by an *x*, and the theoretical strain of bulk copper using the coefficient of thermal expansion. As shown in Figure 7.2, the two curves are similar in shape, but there is a relatively constant error between the theoretical strain values and the measured strain values. This error is attributed to the presence of the silica EFPI inside the copper coating which has a lower coefficient of thermal expansion than that of bulk copper.

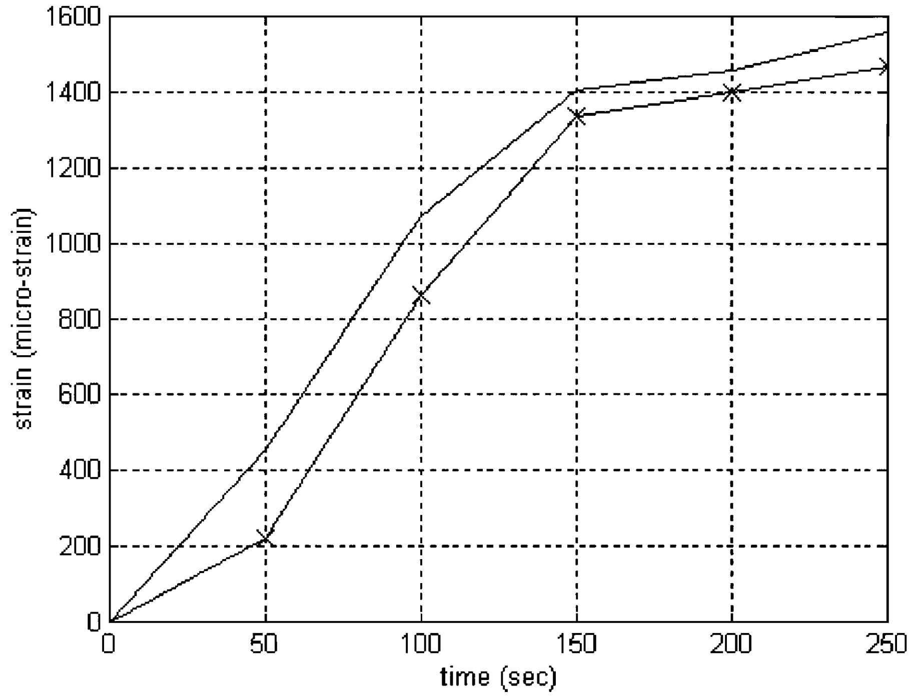

Figure 7.2. Theoretical and measured strain for temperature sensing experiment.

In conclusion, the metal-coated EFPI is a promising temperature sensor, however, prior to implementation of such a device, the thermal characteristics of the entire material system (sensor and coating) should be evaluated. A preliminary treatment of this subject is provided by Sirkis [15,25,26], but adaptations of the models must be made to accommodate the geometry of the EFPI sensor. It should also be noted that temperature will have a significant impact on the performance of the post-damage inspection and corrosion sensors discussed in Chapters 5 and 6. The thermal-apparent strain properties of the sensors must be addressed in future development of these metal-coated sensors.

Chapter 8 - Conclusions

This thesis presented the preliminary development of fiber optic post-damage inspection, corrosion, and temperature sensors constructed with thick metal coatings. An overview of available fiber optic sensor types was provided and a justification for using the extrinsic Fabry-Perot interferometric (EFPI) fiber optic sensor in this research was indicated in Chapter 1. A basic overview of material deformation mechanics was presented in Chapter 2 which provided the basis of operation for the post-damage inspection and corrosion sensing device. Candidate sensor fabrication techniques were discussed in Chapter 3 which allow the deposition of thick metal coatings on optical fiber sensors and the fabrication of the test sensors was described in Chapter 4.

Chapters 5-7 addressed the use of the thick metal-coated EFPI sensors in several different applications. A post-damage inspection sensor was presented in Chapter 5 which uses plastic strains induced in the metal coating material to provide a memory to the sensor of previously encountered peak strains. Using the post-damage inspection sensor results, a fiber optic corrosion sensor was demonstrated in Chapter 6 which exploits the residual strains retained in the coating material of the post-damage inspection sensor, and the relationship between the magnitude of these strains and the thickness of the coating. Finally, in Chapter 7, the temperature characteristics of the thick metal-coated sensors was briefly explored. Sections 8.1-8.3 summarize the development of these sensors, indicates potential areas of future work for their commercial development, and provides potential applications of the sensor types.

8.1 Fiber Optic Post-Damage Inspection Sensor

In many instances, on-line monitoring of strain sensors is either undesirable or impossible. Presented in this thesis has been the development of a fiber optic post-damage inspection sensor which, due to the plastic properties of the thick metal coating of the sensor, possess a memory regarding previously encountered strain events. An elastic, linear hardening deformation model was discussed in Chapter 2 which provides insight into the performance of the sensor. The elastic, linear hardening model seems appropriate to describe the operation of the EFPI sensor with an 80 micrometer thick copper coating due to the linear peak applied strain versus residual strain relationship obtained for the sensor type (shown in Figure 5.5). The EFPI sensors which were tested with a 40 micrometer thick copper coating yielded a peak applied strain versus residual strain relationship that possessed a noticeable upward concavity which indicates that, at best, an elastic, non-linear hardening model is required to describe the deformation properties of the sensor. Hence, in the experimental investigation conducted in Chapter 5, it appeared that the thicker the metal coating, the more valid the elastic, linear hardening model became. Thinner coated sensors seem to dictate the use of elastic, non-linear hardening models to describe their deformation properties.

The proposed post-damage inspection sensor could be used for a variety of applications, from aerospace to civil infrastructure. The sensor could be used to record peak strains during a rapid event, such as a ballistic impact. Additional aerospace uses could be for measuring peak levels of structural deflection during in-service operations. A representative civil infrastructure application could be to attach the sensor to bridges in earthquake-prone regions which would allow post-detection of peak displacements encountered by a structure during earthquakes, high winds, and other phenomena, and provide valuable information to engineers and scientists in designing future structures for such environments. Although it was not researched in this thesis, residual strains can also be retained by the sensor due to large thermal events [13]; hence, the post-damage inspection sensor may be useful in monitoring peak temperatures of a dynamic event when it is undesirable to have electronic support equipment in the location of the sensor.

To develop the sensor for commercial applications, metal coating technologies could be further explored which provide a means to control the yield strength of a deposited coating. Furthermore, development of more exact models which describe the performance of the sensor could be evaluated. As previously mentioned in Chapter 2, Sirkis and Dasgupta [15] have performed preliminary theoretical work in this area which relates residual strain of the sensor to peak encountered stress. However, in real-world applications of the sensor, peak strain versus residual strain relationships would likely be of more interest which would require modeling of the deformation properties of the sensor for specific applications. Finally, a desirable trait of the thicker coated sensor was the apparent close observance of the elastic, linear hardening model which the sensor exhibited. As discussed in Chapter 2, this provides many benefits to the practical use of the sensor in that residual strain is a linear function of peak applied strain. Through the preliminary developmental work presented here, the proposed thick metal-coated fiber optic sensing approach seems promising for a variety of post-damage inspection and detection applications.

8.2 Fiber Optic Corrosion Sensor

As with the post-damage inspection sensor, the proposed fiber optic corrosion sensor could be valuable to a variety of aerospace, hydrospace and civil infrastructure applications. In the experimental work documented in Chapter 6, the tested corrosion sensors provided a mean error of 4.5 % in their ability to accurately measure the relaxation of residual strains in their coatings during the accelerated corrosion tests.

The corrosion sensor provides periodical addressing capabilities to the in-service use of the sensor, which again can reduce the per-channel cost of implementing the sensor type. The corrosion sensor could be used to monitor the corrosion of bridges, dams, aircraft, and ships, by selecting the appropriate coating material and implementation procedure.

Future work for developing the corrosion sensor closely parallels that of the post-damage inspection application of the sensor. Important to the further development of the corrosion sensors is the identification of application specific coating materials and their implementation via coating processes. Additionally, the spatial distribution of the residual strains in the sensor coating must be studied to insure accurate interpretation of the data provided by the sensor which will be a challenging task since the strain distribution is undoubtedly a function of the coating material and pre-straining process. However, due to the significant benefits offered by the fiber optic corrosion sensor, such as quick response, small size, and geometrical flexibility, the additional development of the corrosion sensor may be warranted.

8.3 Fiber Optic Temperature Sensor

A third application of the thick metal-clad fiber optic sensors constructed for this research is that of temperature sensing. Although a very rough analysis of the temperature sensing potential of the metal-coated sensors was performed, indications are that it has potential to be used in this respect. As mentioned in Chapter 7, the coefficient of thermal expansion

(CTE) of bulk copper is 16.74 microstrain/°C, whereas the copper coated EFPI sensor demonstrated an approximate CTE of 15.5 microstrain/°C. The approximate CTE of the coated sensor element appeared nearly linear when compared with the temperature reported by the thermocouple which was used for comparison purposes in the experiments. The observed errors can be attributed to experimental error and response time differences between the thermocouple and metal-coated EFPI sensor; the deviations in linearity between the temperature measured by the thermocouple and strain reported by the metal-coated sensor suggest a mean error of approximately 5°C in the experiments. However, response time differences between the thermocouple and metal-coated sensor can again explain much of this error, furthermore, the thermal-apparent strain properties of the metal-coated sensor may be inherently non-linear but repeatable and therefore could be characterized via an empirical characterization of the temperature sensing properties of the sensor. Future work to develop the metal-coated sensor for commercial and laboratory applications would require further investigations into the response time and temperature measurement resolutions provided by the metal-coated sensor.

A more important result of the temperature sensing research than the use of the sensor element as a temperature sensor is simply the presence of the thermal apparent strain reported by the metal-coated sensor. The temperature sensitivity property of the metal-coated sensor must be thoroughly addressed prior to real-world implementations of either the post-damage inspection or corrosion sensors. But, the linearity observed in the temperature response of the metal-coated sensor indicate that correction for thermal effects in the operation of the sensors is certainly achievable.

References

[1] Dakin, J. and B. Culshaw, **Optical Fiber Sensors: Principles and Components**, Artech House, MA, 1988.

[2] Vengsarkar, A., "Fiber Optic Sensors: A Comparative Evaluation," **The Photonics Design and Applications Handbook**, pp. 114-116, 1991.

[3] Giallorenzi, T.G., J.A. Bucaro, A. Dandridge, G.H. Sigel, Jr., J.H. Cole, S.C. Rashleigh, and R.G. Priest, "Optical Fiber Sensor Technology," *IEEE Journal of Quantum Electronics*, Vol. QE18, No. 4, pp. 626-664, April 1982.

[4] Sirkis, J.S. and H.W. Haslach, Jr., "Interferomeric Strain Measurement by Arbitrarily Configure, Surface-Mounted, Optical Fibers," *Journal of Lightwave Technology*, Vol. 8, No. 10, pp. 1497-1503, October 1990.

[5] Farahi, F., D.J. Webb, J.D.C. Jones, and D. Jackson, "Simultaneous measurement of temperature and strain: cross-sensitivity considerations," *Journal of Lightwave Technology*, Vol. 8, No. 2, p. 138, 1990.

[6] Murphy, K., M. Gunther, A. Vengsarkar, R. Claus, "Extrinsic Fabry-Perot Interferometer," U.S. Patent Pending, Virginia CIT case 90-3479, licensed to F&S, 1992.

[7] Murphy, K., M. Gunther, A. Vengsarkar, R. Claus, "Quadrature phase-shifted, extrinsic Fabry-Perot optical fiber sensors," *Optics Letters*, Vol. 16, No. 4, Feb. 1991.

[8] Murphy, K., M. Miller, C. Koob, R. Claus, "Measurement of Fatigue Crack Opening Displacements in Mullite Ceramics," *J. Intel. Mat. Syst. and Struct.*, Aug. 1991.

[9] Claus, R., M. Gunther, A. Wang, K. Murphy, "Extrisic Fabry-Perot Sensor for Strain and COD Measurements from -200° to 900°C," *Smart Materials and Structures*, Vol. 1, pp. 237-242, 1992.

[10] Bhatia, V., *Signal Processing Techniques for Optical Fiber Sensors Using White Light Interferometry*, Masters Thesis, Bradley Department of Electrical Engineering, Virginia Polytechnic Institute and State University, September 1993.

[11] Calladine, C.R., **Engineering Plasticity**, Pergamon Press, Oxford, England, 1969.

[12] Dowling, N.E., **Mechanical Behavior of Materials: Engineering Methods for Deformation, Fracture, and Fatigue**, Prentice Hall, Englewood Cliffs, NJ, 1993.

[13] Sirkis, J.S. and A. Dasgupta, "Thermal Plastic Metal Coatings on Optical Fiber Sensors," *SPIE Fiber Optic Smart Structures and Skins IV*, Vol. 1588, pp. 88-99, 1991.

[14] **NACE: Basic Corrrosion Course**, National Association of Corrosion Engineers, Sixth Printing, Houston, TX, 1975.

[15] Sirkis, J.S. and A. Dasgupta, "Analysis of a Damage Sensor Based on Elastic-Plastic Metal Coatings on Optical Fibers," *Journal of Lightwave Technology*, Vol. 11, No. 8, pp. 1385-1393, 1993.

[16] Pierson, H.O., **Handbook of Chemical Vapor Deposition (CVD): Principles, Technology, and Applications**, Noyes Publications, Park Ridge, NJ, 1992.

[17] **Metal Finishing. Guidebook and Directory Issue**, M. Murphy, ed., Vol. 92, No. 1A, Metal Finishing, NY, NY, 1994.

[18] Zeakes, J., *Personal Communication*, March 31, 1994.

[19] Von Fraunhofer, J.A., **Basic Metal Finishing**, Paul Elek Ltd., London, England, 1976.

[20] Sherrer, D., *Personal Communication*, April 29, 1994.

[21] Parthasaradhy, N.V., **Practical Electroplating Handbook**, Prentice Hall, Englewood Cliffs, NJ, 1989.

[22] Poland, S.H., M.S. Miller, R.G. May, and R.O. Claus, "Experimental verification of embedded optical fiber data bus survivability enhancement using optical fiber sensors," *SPIE Conference on Smart Materials and Structures*, Boston, Mass, Sept. 1993.

[23] Jones, M.E., V. Bhatia, K.A. Murphy, R.O. Claus, J.L. Grace, S.H. Poland, T.A. Tran, and J.A. Greene, "Multi-Component and Residual Strain Field Characterization Using a Quadrature Phase-Shifted EFPI," International Conference on Intelligent Materials, Williamsburg, VA, January 1994.

[24] Scherrer, D., *Personal Communication*, May 8, 1994.

[25] Sirkis, J.S., "A unified approach to phase-strain-temperature models for smart strucure interferometric optical fiber sensors: Part I," *Opt. Eng.*, Vol. 32, No. 4, pp. 752-761, 1993.

[26] Sirkis, J.S., "A unified approach to phase-strain-temperature models for smart strucure interferometric optical fiber sensors: Part II," *Opt. Eng.*, Vol. 32, No. 4, pp. 762-772, 1993.

Vita

Stephen H. Poland was born in Norfolk, Virginia on August 11, 1966. He graduated with a B.S. in Electrical Engineering from Virginia Polytechnic Institute and State University in May 1992. He joined the Fiber and Electro-Optics Research Center at Virginia Tech as a Research Assistant in December of 1991, and began working for Fiber & Sensor Technologies, Inc., as a Research Scientist in May 1993. Mr. Poland received his M.S. in Electrical Engineering from the Bradley Department of Electrical Engineering at the Virginia Polytechnic Institute and State University in 1994.

Mr. Poland is member of the Institute of Electrical and Electronics Engineers (IEEE) and the Optical Society of America (OSA). His professional interests include fiber optic sensing, digital signal processing, neural networks and fiber optic communications.